UNIVERSITÀ DEL PIEMONTE ORIENTALE

UNIVERSITÀ DEGLI STUDI DEL PIEMONTE ORIENTALE

"AMEDEO AVOGADRO"

Dipartimento di Scienze e Innovazione tecnologica

Corso di Laurea Magistrale in Scienze Chimiche

Advanced Yb^{3+}/Er^{3+}-TiO_2 architectures: mastering upconversion for NIR-to-visible light harvesting

Relatrice:

Prof.ssa Enrica Gianotti

Firmato digitalmente da Enrica Gianotti
Data: 30.06.2026 19:55:33 CEST
Organizzazione: UNIVERSITA' DEGLI STUDI DEL PIEMONTE ORIENTALE/01943490027

Correlatrice:

Prof.ssa Ivana Miletto

Secondo correlatore:

Dott. Gioele Ancora

Giulia Meneghel

Candidata: Giulia Meneghel

Matricola: 20045692

Anno accademico 2025/2026

Index

Abstract 4

1. Introduction 6

1.1 Aim of this work 6

1.1 Titanium dioxide (TiO_2) 7

1.1.1 Synthetic approach 7

1.1.2 Photocatalytic activity 8

1.1.3 TiO_2 limitations 9

1.2 Rare Earth Elements (REEs) 10

1.2.1 Upconversion luminescence (UCL) 10

1.2.1.1 Er^{3+}/Yb^{3+} UCL mechanisms 13

1.3 TiO_2 doping for band gap modification 14

1.3.1 Dye-sensitization 16

1.3.1 Metal and noble metal doped TiO_2 17

1.3.1.1 Silver (Ag) doping 18

1.3.2 Non-metal doped TiO2 19

1.3.2.1 Nitrogen doping 20

1.4 Photodynamic therapy (PDT) 21

2. Materials and Methods 24

2.1 Synthesis of Ag-, Er-, Tm-, Yb- doped TiO_2 24

2.3 Physico-chemical Characterization 26

2.4 Reactive oxygen species generation 28

3. Results and discussion 30

3.1 Ag-, Er-, Tm-, Yb- doped TiO_2 30

3.1.1 X-Ray powder diffraction (XRPD) 30

3.1.2 X-Ray fluorescence spectroscopy (XRF) 34

3.1.3 Field emission scanning electron microscopy and Scanning transmission electron microscopy 36

3.1.4 Dynamic light scattering 38
3.1.5 Diffuse reflectance UV-Vis-NIR spectroscopy (DR UV-Vis-NIR)..... 39
3.1.6 Photoluminescence (PL) spectroscopy..... 45
3.1.6.1 Emission spectra..... 46
3.1.6.2 Excitation spectra 49
3.1.7 Upconversion (UC) 52
3.1.8 Reactive oxygen species (ROS) generation tests 55
4. Conclusions..... 62
References 64

Abstract

In recent years, the development of multifunctional nanomaterials capable of responding to external stimuli has garnered significant attention in materials chemistry, owing to their promising applications in environmental remediation, energy conversion, and nanomedicine. Among various semiconductors, titanium dioxide (TiO_2) stands out as one of the most widely investigated photocatalysts due to its high photoactivity, chemical stability, and low toxicity. However, its efficiency is severely constrained by its wide band gap, which restricts its activation exclusively to the UV region, and by the rapid recombination of photogenerated electron-hole pairs.

This thesis work aims to overcome these limitations through the design, synthesis, structural characterization, and photocatalytic evaluation of TiO_2 nanoparticles co-doped with lanthanides (Er^{3+} and Yb^{3+}) and silver (Ag). The primary objective is to develop a near-infrared (NIR)-responsive nanoplatform capable of generating reactive oxygen species (ROS) under NIR excitation (980 nm), thereby combining the upconversion luminescence (UCL) mechanism of the Er^{3+}/Yb^{3+} pair with the structural and electronic properties induced by silver. This approach opens up new avenues for potential applications in photodynamic therapy (PDT).

The materials were synthesized via the sol-gel method, comparing the effects of two distinct post-synthetic treatments: Method 1 (incorporating a washing step) and Method 2 (without washing). X-ray powder diffraction (XRPD) analysis confirmed that all nanoparticles predominantly consist of the anatase crystalline phase, showing no phase alterations induced by either doping or washing. Morphological and dimensional investigations (FE-SEM, STEM, and DLS) revealed spherical nanoparticles with primary particle sizes ranging between 50 and 100 nm, which exhibit a tendency to form macro-aggregates in aqueous media that can be removed through filtration. X-ray fluorescence (XRF) spectroscopy demonstrated that Method 2 (unwashed) is significantly more effective at retaining the nominal loading of dopants compared to the washed counterparts, while successfully maintaining the optimal Yb/Er molar ratio of approximately 10 across all co-doped systems.

Optical characterization via Diffuse Reflectance spectroscopy (DR UV-Vis-NIR) validated the successful incorporation of lanthanide ions into the matrix through the detection of their characteristic intra-4f absorption bands, most notably the peak at 975

nm. The introduction of silver induced a pronounced red-shift in the absorption edge of TiO_2, extending its optical response into the visible light region. This effect was found to be more pronounced in the unwashed samples (Method 2) due to higher dopant retention. This behavior is associated with the surface migration of metallic silver and the formation of a Schottky barrier at the metal-semiconductor interface, which is ideal for suppressing charge carrier recombination.

Finally, the efficiency of ROS production was evaluated through photo-oxidation tests using 1,3-diphenylisobenzofuran (DPBF) as a chemical probe. While visible light irradiation at 520 nm did not yield significant reactive species production, NIR excitation at 980 nm successfully induced progressive degradation of DPBF in the rare-earth-doped samples, confirming the upconversion-mediated activation of the semiconductor. Among the investigated formulations, the TiO_2_Ag_Er_Yb_2 sample (Method 2) exhibited the highest photocatalytic efficiency, resulting in a 17% decrease in DPBF absorbance after 60 minutes of irradiation. This outcome confirms the successful synergy between lanthanide co-doping and silver incorporation, validating the synthesized material as a highly promising nanostructure for NIR-light-driven biomedical applications.

1. Introduction

1.1 Aim of this work

In recent years, multifunctional nanomaterials have attracted considerable attention in materials chemistry due to their ability to combine different chemical components within a single system, thereby integrating properties that cannot be achieved by individual constituents alone. This strategy has enabled the development of advanced materials capable of responding to external stimuli and performing multiple functions simultaneously. Within this field, photoactive nanomaterials are of particular interest because of their ability to convert light into chemical or physical responses, with applications in environmental remediation, energy conversion, and nanomedicine. In particular, semiconductor-based systems that generate reactive oxygen species (ROS) under light irradiation are widely investigated for photocatalytic purposes.[1–3]

Among these materials, titanium dioxide (TiO_2) is one of the most studied photocatalysts due to its high photoactivity, low cost, low toxicity, and good chemical and thermal stability.[4] However, its practical application is limited by its large band gap, which restricts photo-response to the UV region, and by the rapid recombination of photogenerated electron–hole pairs, which reduces quantum efficiency. To overcome these limitations, various modification strategies have been explored, including metal and non-metal doping, surface sensitization with dyes, incorporation of noble metal nanoparticles, and coupling with narrow band gap semiconductors.[2–4]

The present work focuses on the synthesis, characterization and photocatalytic evaluation of TiO_2 nanoparticles co-doped with Er^{3+}, Yb^{3+} and Ag. The proposed material was designed to combine the photocatalytic properties of TiO_2 with the NIR-to-visible upconversion capability of the Er^{3+}/Yb^{3+} couple, while Ag doping was introduced to improve the electronic structure of TiO_2 and favour the energy transfer between the lanthanide ions and the semiconductor matrix. The ultimate goal is the development of a NIR-responsive photocatalytic nanoplatform capable of producing reactive oxygen species under 980 nm excitation, with potential application in photodynamic therapy.

1.1 Titanium dioxide (TiO_2)

TiO_2 is a semiconducting material that has attracted considerable interest because of its unique combination of physical and chemical properties. Its high thermal stability, non-toxicity, low cost, natural abundance and its unique photocatalytic activity under UV light make it a suitable material for a broad range of applications spanning from environmental remediation and energy conversion to biomedical technologies.[8]

TiO_2 can crystallize in four main polymorphic phases: anatase, rutile, brookite, and TiO_2-bronze (monoclinic). Figure 1 schematically illustrates the crystal structures of these polymorphs.[9] Among these phases, anatase, with a band gap of approximately 3.2 eV, is generally considered the most photocatalytically active because of its favourable band bending characteristics, which promote the trapping of photogenerated holes at the surface and consequently enhance the formation of reactive radical species.[10]

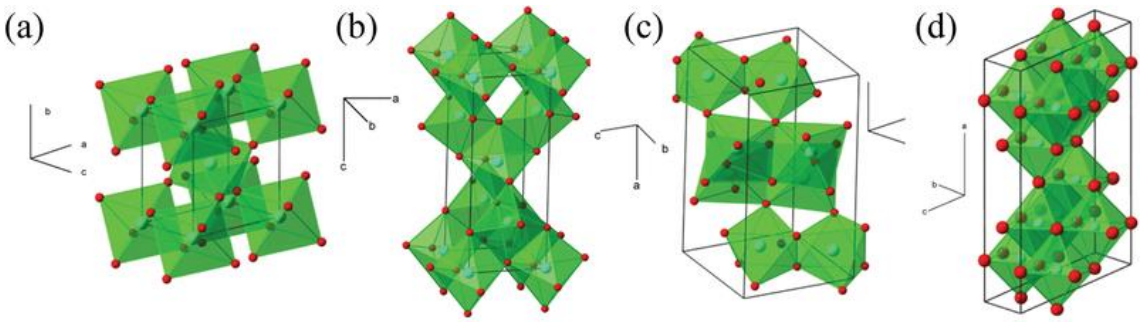

Figure 1. *Schematic representation of the four TiO_2 polymorphs: Rutile, Brookite, Anatase and TiO_2-bronze.*

1.1.1 Synthetic approach

The crystalline phase and morphology of TiO_2 nanoparticles are strongly influenced by synthesis parameters, including temperature, pH, pressure, and precursor concentration. Low-temperature synthesis (≤ 500 °C) generally favours the formation of the anatase phase, whereas increasing the synthesis temperature promotes the transformation of anatase into rutile. Acidic conditions stabilize the anatase phase and typically result in spherical particles, while alkaline environments favour anisotropic crystal growth. Furthermore, precursor concentration plays a crucial role in determining particle size and the extent of agglomeration, which directly affect the available surface area and the efficiency of charge transfer processes.[8]

Among the available synthesis methods, the sol-gel technique is particularly attractive because it provides a high degree of control over particle size, morphology, and microstructure throughout the synthesis process, making it particularly suitable for the preparation of nanoparticles and thin films. Such control contributes to enhanced phase stability and improved photocatalytic performance by reducing charge carrier recombination. In addition, the process combines relatively low energy consumption with simple and inexpensive equipment while allowing precise control over the structural characteristics of TiO_2 particles.[8,11]

1.1.2 Photocatalytic activity

The photocatalytic activity of TiO_2 originates from the generation of electron-hole pairs following irradiation with UV or near-UV light. The photocatalytic process of TiO_2 begins with the absorption of photons whose energy is equal to or greater than its band gap. This excitation promotes an electron (e^-) from the valence band to the conduction band, leaving behind a positively charged hole (h^+) in the valence band and thus generating an electron–hole pair. The photogenerated charge carriers can undergo three possible pathways. First, the electron and hole may recombine, releasing the absorbed energy as heat. This process is undesirable because it reduces the number of charge carriers available for photocatalytic reactions, thereby lowering the overall efficiency of TiO_2. Second, the charge carriers may become trapped in metastable surface or defect states, which can prolong their lifetime by delaying recombination. Although the exact nature of these trapping states is still under investigation, they have been associated with surface defects, hydroxyl groups, and hydrogen-bonding interactions that modify the surface energy of TiO_2. Finally, if recombination is avoided, the photogenerated electrons and holes migrate to the catalyst surface, where they react with adsorbed electron acceptors and donors. In particular, conduction-band electrons reduce oxygen molecules to form reactive oxygen species (ROS), while valence-band holes oxidize water or surface hydroxyl groups to generate hydroxyl radicals (•OH). These highly reactive species are responsible for the degradation of organic contaminants, water splitting, and numerous other photocatalytic processes. Figure 3 offers a schematic representation of the important processes in TiO_2 photocatalysis: electron–hole pair generation, charge transfer, electron–hole pair recombination in the bulk or at the surface, and electron and hole induced chemistry at the surface.[3,8,9]

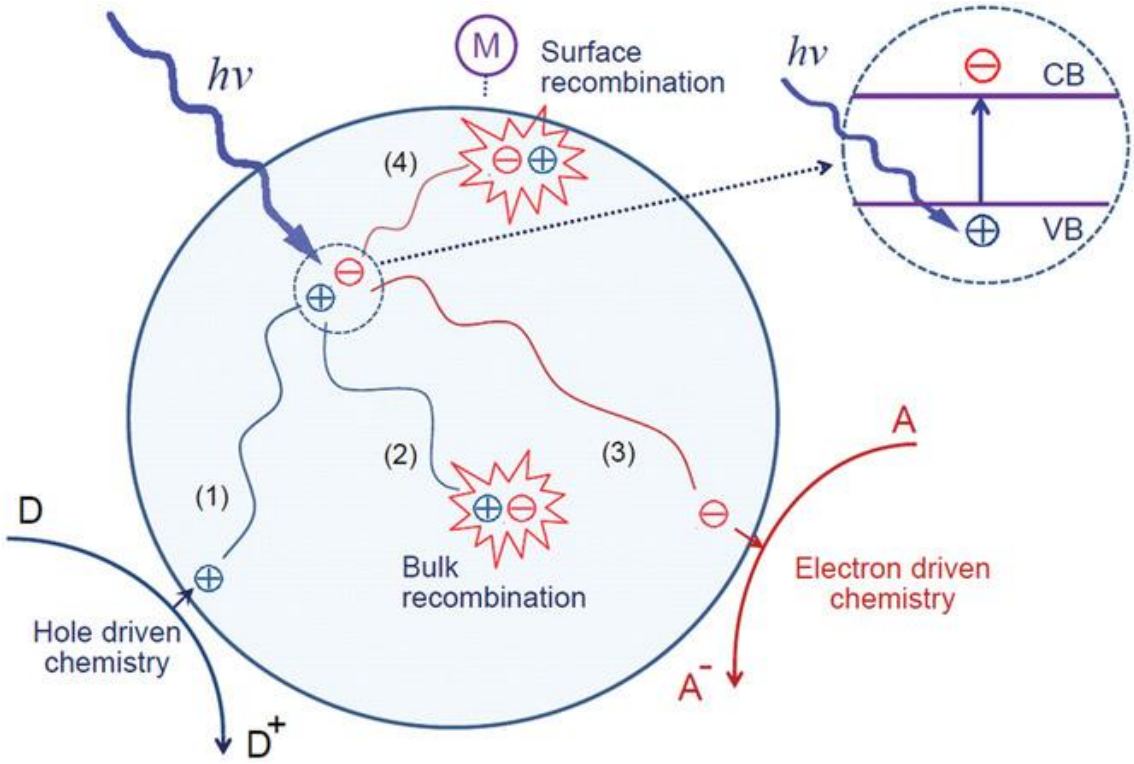

Figure 2. *Schematic representation of important processes in TiO_2 photocatalysis: electron–hole pair generation, charge transfer, electron–hole pair recombination in the bulk or at the surface, and electron and hole induced chemistry at the surface.*[9]

1.1.3 TiO_2 limitations

Despite the numerous advantages of TiO_2, its performance is significantly limited by several intrinsic properties related to its electronic structure and crystal phases. Firstly, the rapid recombination of photogenerated electron–hole pairs that can occur both in the bulk and at the surface of the material and is strongly influenced by defects, impurities, and structural imperfections. As a consequence, the number of charge carriers available for redox reactions is significantly reduced, leading to a low quantum efficiency. In addition, prolonged irradiation may induce photo-corrosion phenomena and gradual surface degradation, while the thermodynamically metastable anatase phase can irreversibly transform into rutile at temperatures above approximately 600–700 °C, resulting in a decrease in photocatalytic activity.

Among all the intrinsic limitations of TiO_2, however, its wide band gap represents the major obstacle to the development of efficient photoactive systems. The anatase phase exhibits a band gap of approximately 3.2 eV, meaning that only ultraviolet photons ($\lambda <$ 387 nm) possess sufficient energy to promote electrons from the valence band to the

conduction band. These characteristics considerably restrict the use of TiO_2 in applications requiring deep light penetration or the use of low-energy radiation.

For this reason, considerable research efforts have been devoted to extending the optical response of TiO_2 towards longer wavelengths. A promising strategy relies on coupling TiO_2 with optically active materials capable of absorbing low-energy radiation and transferring the harvested energy to the semiconductor. Among these materials, rare earth elements (REEs) have attracted particular interest because of their unique upconversion properties, which enable the indirect activation of TiO_2 under near-infrared irradiation.[3,8,12,13]

1.2 Rare Earth Elements (REEs)

Rare Earth Elements (REEs) comprise the fifteen lanthanides, extending from lanthanum (La) to lutetium (Lu), together with scandium (Sc) and yttrium (Y), which are commonly included because of their similar chemical properties. The remarkable optical behaviour of lanthanide ions arises from their unique electronic structure, in which the partially filled 4f orbitals are effectively shielded by the outer filled 5s and 5p shells. As a result, the electronic energy levels are only weakly affected by the surrounding chemical environment, giving rise to characteristic intra-configurational 4f–4f transitions with narrow emission bands, long excited-state lifetimes, and excellent photostability.

These distinctive spectroscopic properties make lanthanide ions ideal candidates for a wide range of optical applications. Among their various optical applications, upconversion luminescence has attracted particular attention because it enables the conversion of low-energy near-infrared photons into higher-energy visible or ultraviolet light through the ladder-like energy levels of selected lanthanide ions. Owing to its high penetration depth, low background autofluorescence, and excellent photostability, this phenomenon has become a key strategy in areas such as bioimaging, photocatalysis, sensing, and phototherapy. The fundamental principles and mechanisms governing upconversion luminescence are discussed in the following section.[4,14]

1.2.1 Upconversion luminescence (UCL)

UCL is a nonlinear optical process in which the sequential absorption of two or more low-energy photons results in the emission of a single photon with higher energy. Unlike conventional fluorescence, where the emitted photon has lower energy than the excitation

light (Stokes emission), upconversion generates anti-Stokes emission, typically converting near-infrared (NIR) excitation into visible or ultraviolet light. This process is made possible by the long-lived intermediate excited states of lanthanide ions, which allow the successive absorption or transfer of excitation energy before radiative relaxation occurs.[15] Efficient upconversion generally requires the combination of three fundamental components (Figure 3):

- Activator (A): the luminescent centre responsible for photon emission after either direct excitation by near-infrared (NIR) irradiation or, more commonly, after receiving excitation energy from a sensitizer.
- Sensitizer (S): an ion capable of efficiently absorbing excitation light at a specific wavelength and transferring the harvested energy to the activator, thereby promoting UCL.
- Host matrix: a crystalline lattice that accommodates both sensitizer and activator ions at appropriate concentrations, enabling the energetic interactions required for the different upconversion pathways.[16]

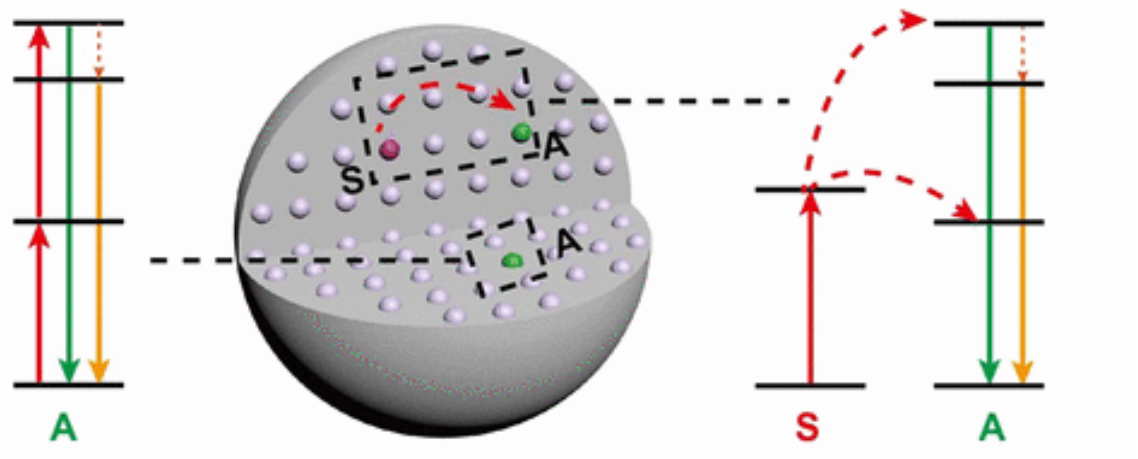

Figure 3. *Lanthanide ions S and A in the host, schematic energy levels of A, and energy transfer from S to A. S stands for sensitizer and A for activator.*[16]

Upconversion can occur through five principal mechanisms: excited-state absorption (ESA), energy transfer upconversion (ETU), cooperative sensitization upconversion (CSU), cross relaxation (CR) and photon avalanche (PA), as illustrated in Figure 4.[15]

- Excited-state absorption (ESA): ESA is the simplest upconversion mechanism, as it involves a single lanthanide ion. The ion first absorbs one excitation photon and

is promoted from the ground state (G) to a long-lived intermediate excited state (E1). Before relaxing back to the ground state, it absorbs a second photon that promotes it to a higher excited state (E2). Radiative relaxation from E2 then produces the upconverted emission. Because this mechanism relies on the sequential absorption of photons by a single ion, it can occur only in lanthanides with suitable ladder-like energy levels, such as Er^{3+}, Ho^{3+}, Tm^{3+} and Nd^{3+}.

- Energy transfer upconversion (ETU): ETU involves two neighbouring ions: a sensitizer and an activator. The sensitizer first absorbs the excitation photon and stores the energy in its excited state. Instead of emitting light, it transfers this energy to the activator. After two successive energy-transfer events, the activator reaches a higher excited state (E2), from which it relaxes radiatively, producing upconverted emission. Because this mechanism relies on energy transfer between neighbouring ions, its efficiency strongly depends on the distance between sensitizer and activator ions, and therefore on the dopant concentration. ETU is the most efficient and widely exploited upconversion mechanism in lanthanide-doped nanoparticles, particularly in Yb^{3+}/Er^{3+}, Yb^{3+}/Tm^{3+}, and Yb^{3+}/Ho^{3+} systems excited at approximately 975 nm.
- Cooperative sensitization upconversion (CSU): CSU is a three-ion process involving two sensitizer ions and one activator ion. After excitation, both sensitizers simultaneously transfer their stored energy to the activator, promoting it directly to a higher excited state. The activator subsequently relaxes by emitting an upconverted photon. Because the simultaneous transfer of energy from two ions is intrinsically unlikely, CSU is much less efficient than ESA or ETU. However, its highly localized excitation can be advantageous for high-resolution imaging applications.
- Cross-relaxation (CR): Cross-relaxation is a non-radiative energy transfer process that occurs between two neighbouring lanthanide ions. During this interaction, an excited ion transfers part of its energy to a nearby ion in the ground or in a lower excited state, resulting in the simultaneous redistribution of energy between the two ions. Depending on the energy levels involved, cross-relaxation may either enhance or reduce the upconversion emission by changing the population of the emitting states. This mechanism is particularly relevant in highly doped systems, where the short distance between neighbouring lanthanide ions increases the probability of ion-ion interactions.

- Photon avalanche (PA): Photon avalanche is a nonlinear upconversion mechanism that occurs only when the excitation power exceeds a threshold value. Initially, only a few ions are promoted to a metastable excited state. These ions undergo excited-state absorption and, through cross-relaxation with neighbouring ions, generate additional excited ions. This positive-feedback process continuously increases the excited-state population, leading to a rapid, avalanche-like increase in luminescence intensity. Consequently, PA exhibits a well-defined excitation threshold, a relatively slow build-up time, and a very strong dependence of the emission intensity on the excitation power.[2,16]

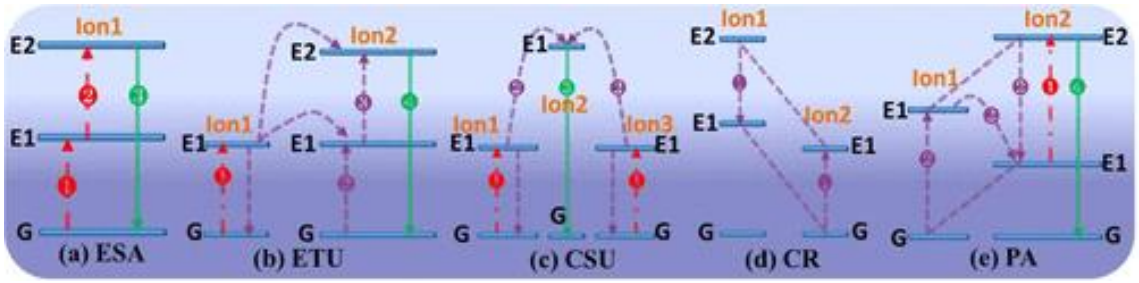

Figure 4. *Principal UC processes for lanthanide-doped UCNPs: (a) excited-state absorption (ESA), (b) energy transfer upconversion (ETU), (c) cooperative sensitization upconversion (CSU), (d) cross relaxation (CR), and (e) photon avalanche (PA). The red, violet, and green lines represent photon excitation, energy transfer, and emission processes, respectively.*[2]

1.2.1.1 Er^{3+}/Yb^{3+} UCL mechanisms

Among the different sensitizer–activator combinations, the Yb^{3+}/Er^{3+} pair is the most extensively investigated and one of the most efficient upconversion systems.[16] Its success mainly arises from the electronic structure of Yb^{3+}, which possesses only two energy levels, the ground state ($^2F_{7/2}$) and a single excited state ($^2F_{5/2}$).[17] The energy gap between these two levels closely matches the energy of a 980 nm photon, allowing Yb^{3+} to efficiently absorb near-infrared radiation. In addition, the excited state of Yb^{3+} is in good resonance with the $^4I_{11/2}$ level of Er^{3+}, making energy transfer between the two ions highly efficient. Minor energy mismatches can be compensated by phonon-assisted energy transfer, further improving the upconversion efficiency.[16,18]

The upconversion process, reported in Figure 5, is initiated when Yb^{3+} absorbs a 980 nm photon and is promoted from the $^2F_{7/2}$ ground state to the $^2F_{5/2}$ excited state. Instead of

emitting light directly, the excited Yb^{3+} ion transfers its energy non-radiatively to a neighbouring Er^{3+} ion and simultaneously returns to its ground state. This first energy-transfer event promotes Er^{3+} from its ground state ($^4I_{15/2}$) to the intermediate $^4I_{11/2}$ level. A second 980 nm photon is then absorbed by another Yb^{3+} ion, which again transfers its energy to the already excited Er^{3+} ion. As a result, Er^{3+} is promoted from the $^4I_{11/2}$ level to higher excited states, such as $^4F_{7/2}$. From this level, the ion rapidly undergoes non-radiative relaxation to lower excited states ($^2H_{11/2}$, $^4S_{3/2}$, and $^4F_{9/2}$), from which radiative relaxation to the ground state generates the characteristic upconversion emission. In particular, the transitions $^2H_{11/2}/^4S_{3/2} \rightarrow {}^4I_{15/2}$ produce green emission (approximately 520–550 nm), whereas the $^4F_{9/2} \rightarrow {}^4I_{15/2}$ transition is responsible for the red emission around 650 nm.

Because the excitation energy is accumulated through two successive energy-transfer events rather than by direct absorption of multiple photons by Er^{3+}, the Yb^{3+}/Er^{3+} couple exhibits significantly higher upconversion efficiency than Er^{3+} alone. For this reason, the Yb^{3+}/Er^{3+} pair has become the most widely used upconversion system, and several approaches, including host optimization, core–shell structures, co-doping strategies and plasmonic enhancement, have been investigated to further improve its luminescence efficiency.[16]

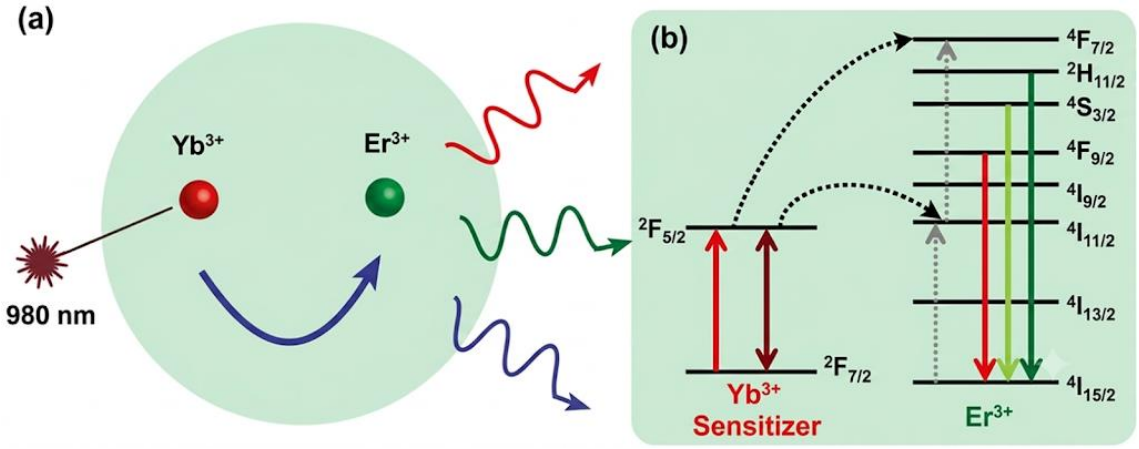

Figure 5. *Schematic representation of Er^{3+}/Yb^{3+} UCL mechanism.*

1.3 TiO_2 doping for band gap modification

As discussed in the previous sections, the combination of TiO_2 with upconverting lanthanide ions offers the possibility of converting deeply penetrating NIR radiation into visible emission. However, the visible photons generated by Er^{3+}-based upconversion

alone are not sufficient to efficiently activate pristine TiO_2, whose wide band gap (~3.2 eV) restricts its photo-response mainly to the UV region. Therefore, although the incorporation of lanthanides extends the excitation wavelength of the overall system, the photocatalytic efficiency remains limited unless the electronic structure of TiO_2 is also modified.

Considerable research efforts have focused on band gap engineering strategies aimed at extending the optical absorption of TiO_2 towards the visible region. These approaches generally rely on the introduction of new electronic states within the band gap or on the modification of the conduction and valence band positions, thereby enabling the activation of the semiconductor under lower-energy irradiation. A schematic comparison of the electronic band structures of pristine and doped TiO_2 is presented in Figure 6.[8,12]

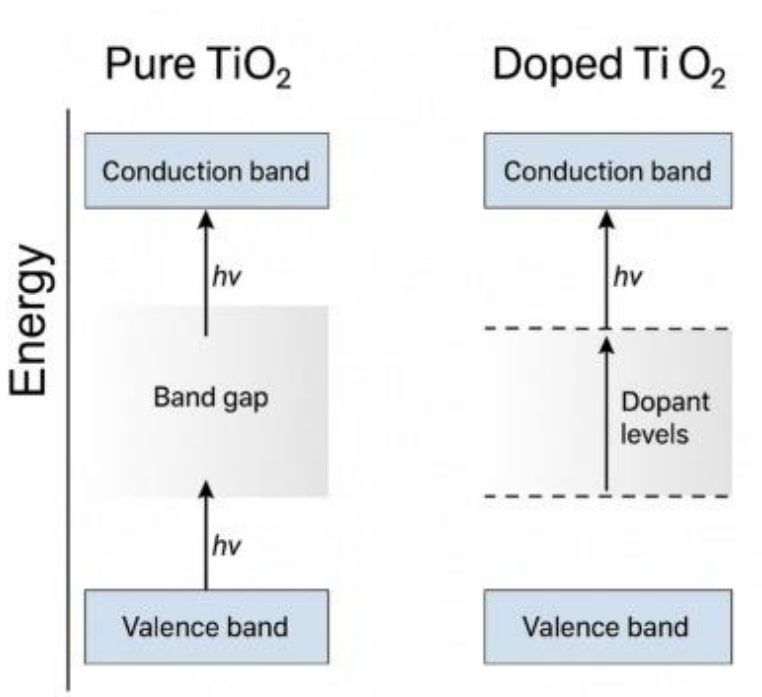

Figure 6. *Schematic illustration of the electronic band structure of pure TiO_2 (left) and doped TiO_2 (right).*[8]

Some of the promising strategies of TiO_2 band gap modification are reported in the following sections.

1.3.1 Dye-sensitization

Dye sensitization represents one of the most established strategies for extending the optical response of TiO_2 beyond its intrinsic band gap. In this approach, dye molecules absorb photons in the visible region and are promoted to an excited state. From this state, they can inject electrons into the conduction band of TiO_2, effectively bypassing the wide band gap limitation of the semiconductor. In this way, the dye acts as a light-harvesting antenna, while TiO_2 functions as an electron acceptor that supports charge separation and drives photocatalytic reactions (Figure 7).

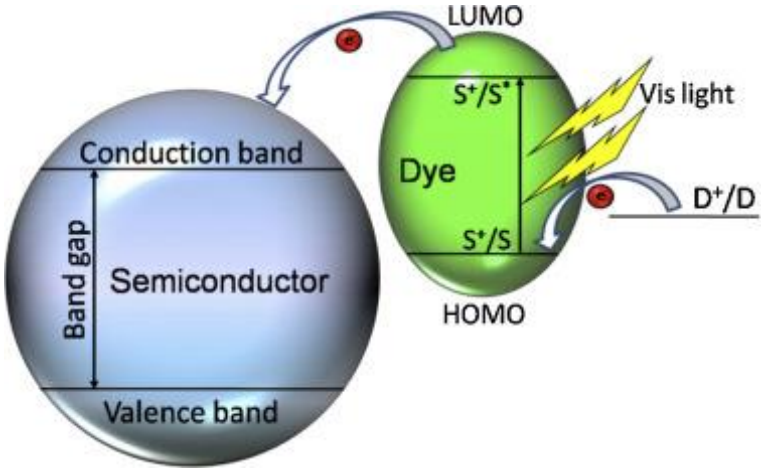

Figure 7. *Mechanism of dye sensitized semiconductor photocatalysis.*[12]

The main advantage of dye sensitization is that it allows the use of low-energy visible light to activate TiO_2, significantly expanding its applicability in photocatalysis and solar-energy conversion. In addition, the separation between light absorption (dye) and catalytic function (TiO_2) can improve charge separation efficiency compared to direct excitation of the semiconductor.

However, dye-sensitized systems also present important limitations. The dye molecules are often not stable under prolonged irradiation and can undergo photodegradation, leading to a gradual loss of activity. Furthermore, recombination of charge carriers can still occur if electron injection into TiO_2 is not sufficiently fast or efficient, reducing the overall photocatalytic performance. For these reasons, dye sensitization is effective but often requires additional stabilization strategies to ensure long-term operation.[12]

1.3.1 Metal and noble metal doped TiO_2

Metal doping is a widely used strategy to overcome the TiO_2 band gap limitation. By introducing metal species into the TiO_2 structure, either as substitutional or interstitial dopants, it is possible to modify its electronic structure and extend its absorption toward the visible region. Metal dopants interact with the Ti 3d orbitals, introducing new electronic states within the band gap or shifting the band edges, which can effectively reduce the band gap and improve light harvesting. In addition, metal ions with suitable electronic energy levels can act as electron traps, capturing photogenerated electrons and thereby reducing electron–hole recombination. This enhances charge separation and improves photocatalytic efficiency by facilitating the migration of charge carriers toward surface redox reactions (Figure 8).

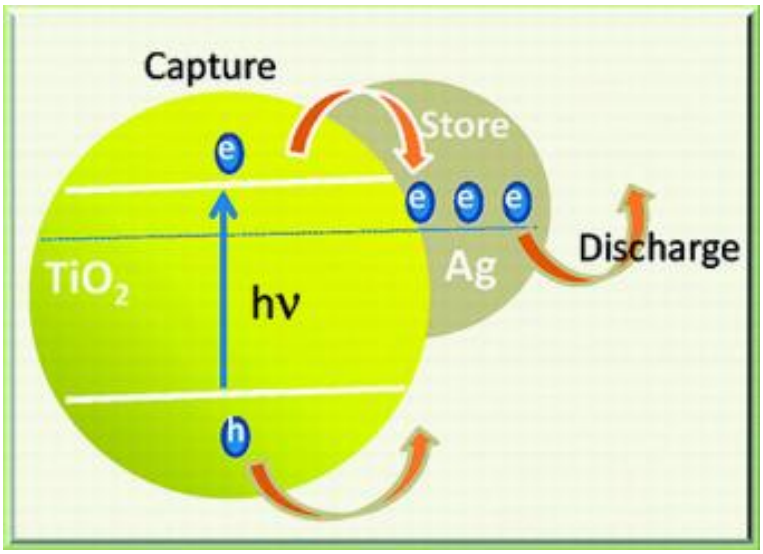

Figure 8. *Electron transfer mechanism in silver loaded TiO_2.*[12]

Among metal dopants, noble metals such as Ag, Au, Pt, and Pd play a particularly important role due to their strong ability to enhance interfacial charge transfer. These metals can act as efficient electron sinks, increasing the lifetime of photogenerated charge carriers and improving overall photocatalytic performance. At the TiO_2 interface, noble metals can form Schottky junctions, which create an internal electric field that drives directional electron transfer from TiO_2 to the metal, further suppressing recombination and promoting surface reactions. In addition, noble metal nanoparticles can exhibit localized surface plasmon resonance (LSPR), which enhances visible-light absorption

through strong local electromagnetic field effects and can contribute to additional electron excitation processes.

The main advantages of metal and noble metal doping are improved visible-light absorption, enhanced charge separation, and increased photocatalytic activity. However, these systems also present limitations, including the possible introduction of recombination centres at high dopant concentrations, potential instability of metal nanoparticles under irradiation, and increased material cost, particularly for noble metals.[3]

1.3.1.1 Silver (Ag) doping

Silver (Ag) is one of the most promising noble metal dopants for TiO_2 modification and is widely regarded as a benchmark system among metal-modified photocatalysts. Its relevance arises from its combined electronic, optical, and biological properties, which make Ag a multifunctional enhancer of TiO_2 performance in photocatalysis and biomedical applications. At the nanoscale, silver nanoparticles (AgNPs) exhibit localized surface plasmon resonance (LSPR), high surface reactivity, and strong antimicrobial activity, which together contribute to their extensive use in environmental remediation, water treatment, antimicrobial coatings, and biomedical devices. When combined with TiO_2 nanoparticles, AgNPs form composite materials with significantly improved functional performance compared to pristine TiO_2.[13,19]

Under irradiation, TiO_2 generates electron–hole pairs; however, their rapid recombination limits photocatalytic efficiency. Silver nanoparticles act as efficient electron sinks, capturing photogenerated electrons from the conduction band of TiO_2. This process is driven by the formation of a Schottky junction at the Ag/ TiO_2 interface, which promotes directional electron transfer from TiO_2 to Ag after Fermi level equilibration. As a result, charge carriers are spatially separated, with electrons accumulating on Ag while holes remain in TiO_2, significantly suppressing recombination and enhancing the availability of charges for surface redox reactions. In addition, Ag nanoparticles can exhibit localized surface plasmon resonance (LSPR), which enhances visible-light absorption through strong local electromagnetic fields and may contribute to additional photoinduced charge generation. The photocatalytic behaviour of Ag-doped TiO_2 strongly depends on the silver loading. At relatively low concentrations, Ag^+ ions tend to migrate and form silver oxide species on the TiO_2 surface. As the silver content increases and metallic Ag^0 nanoparticles

are formed, photocatalytic activity is significantly enhanced.[20] This improvement is primarily attributed to the increased availability of electron trapping sites, which effectively suppress electron-hole recombination, one of the principal factors limiting the performance of pristine TiO_2. In addition to improving charge separation, silver incorporation decreases the band gap of TiO_2 to approximately 2.89 eV, extending its photo-response into the visible region.[21]

Despite these advantages, Ag–TiO_2 systems also present some limitations. The photocatalytic efficiency is highly dependent on the amount and chemical state of silver, and excessive loading may lead to the formation of recombination centres or less active Ag_2O/AgO phases, reducing performance. In addition, a critical concern is the possible release of Ag nanoparticles or Ag^+ ions during operation, which may result in environmental contamination, alteration of microbial communities, and long-term ecological effects.[8,21]

Overall, silver represents one of the most effective and widely investigated noble metal dopants for TiO_2, owing to its strong ability to enhance charge separation, extend light absorption into the visible region, and improve photocatalytic efficiency even at relatively low loadings.

1.3.2 Non-metal doped TiO_2

Since the early 1990s, non-metal doping has attracted considerable attention as an effective strategy for improving the photocatalytic performance of TiO_2.

Non-metal doping lies in the modifies the TiO_2 band structure through the incorporation of heteroatoms such as carbon, nitrogen, sulphur, and phosphorus. These elements can be introduced into the TiO_2 lattice either by substituting oxygen atoms (substitutional doping) or by occupying interstitial positions within the crystal structure. In both cases, the presence of non-metal dopants leads to the formation of new electronic states within the band gap or to the modification of the valence band edge. Substitutional doping typically introduces localized impurity levels inside the band gap, while interstitial doping promotes the formation of intermediate states that facilitate charge transfer and improve the separation of photogenerated electron–hole pairs. As a consequence, the effective band gap of TiO_2 is reduced and the material becomes active under visible-light irradiation.

The main advantage of non-metal doping is therefore the ability to tune the electronic structure of TiO_2 in a relatively simple and cost-effective way, enabling visible-light activation while maintaining good structural stability. In addition, unlike many metal dopants, non-metal elements generally do not act as strong recombination centres when properly incorporated, which helps preserve or even enhance photocatalytic efficiency.
However, non-metal doping also presents some limitations. The extent of band gap narrowing is often modest and strongly dependent on the dopant concentration and incorporation mode. In some cases, dopants can introduce defect states that act as recombination centres if not properly controlled, reducing photocatalytic performance. Moreover, achieving homogeneous and stable doping can be synthetically challenging, particularly when precise control over substitutional versus interstitial incorporation is required.[3]

1.3.2.1 Nitrogen doping

Among non-metal doping, nitrogen is the most extensively investigated and one of the most promising dopants for TiO_2 modification. Nitrogen was the first non-metal successfully incorporated into the TiO_2 lattice and remains highly attractive due to its comparable atomic radius to oxygen, which enables efficient substitution with minimal lattice distortion.[22] The mechanism of nitrogen doping relies on the modification of the electronic structure of TiO_2 through orbital interactions. In particular, the N 2p orbitals interact with the O 2p states of the valence band, leading to the formation of new electronic states just above the valence band edge. These states effectively narrow the band gap and enable the excitation of electrons under visible-light irradiation. As a result, nitrogen-doped TiO_2 can be activated using lower-energy photons, significantly extending its photocatalytic response beyond the ultraviolet region.[23].
Overall, nitrogen doping significantly enhances the photocatalytic performance of TiO_2 under both visible and ultraviolet irradiation. Its effectiveness arises from its ability to introduce band gap states that enable visible-light activation, combined with the possibility of tuning its incorporation mode, with interstitial nitrogen representing the most favourable configuration for maximizing photocatalytic efficiency.[24]

1.4 Photodynamic therapy (PDT)

Photodynamic therapy (PDT) is a minimally invasive treatment strategy based on the light-triggered generation of reactive oxygen species (ROS). Initially developed for oncological applications, PDT has progressively been extended to other fields, including dermatology, ophthalmology, and antimicrobial photodynamic inactivation.[25,26]

Its mechanism relies on the simultaneous presence of three components: light, molecular oxygen and a photosensitizing agent (PS), a photosensitive chemical that, after its activation with light of a specific wavelength in the presence of molecular oxygen, results in selective tissue damage by having a cytotoxic effect on cancer cells. Individually, these components are not sufficient to produce the photodynamic effect; however, when combined, they can induce localized oxidative damage.[25]

It has been found that PDT work through the following mechanism. The PS absorbs light and transitions from its ground state to an excited singlet state, followed by an intersystem crossing to a relatively long-lived excited triplet state. From this triplet state, the photosensitizer can undergo two parallel photochemical pathways:

- Type I reaction: the photosensitizer transfers an electron or a hydrogen atom to nearby biomolecules or oxygen, generating reactive free radicals such as superoxide and hydroxyl radicals;
- Type II reaction: the photosensitizer transfers its energy directly to ground-state molecular oxygen to produce highly reactive and cytotoxic singlet oxygen.

These two types of reactions occur simultaneously, but Type 2 is believed to be the predominant pathway. A schematic representation of this two mechanisms is reported in Figure 9.[27]

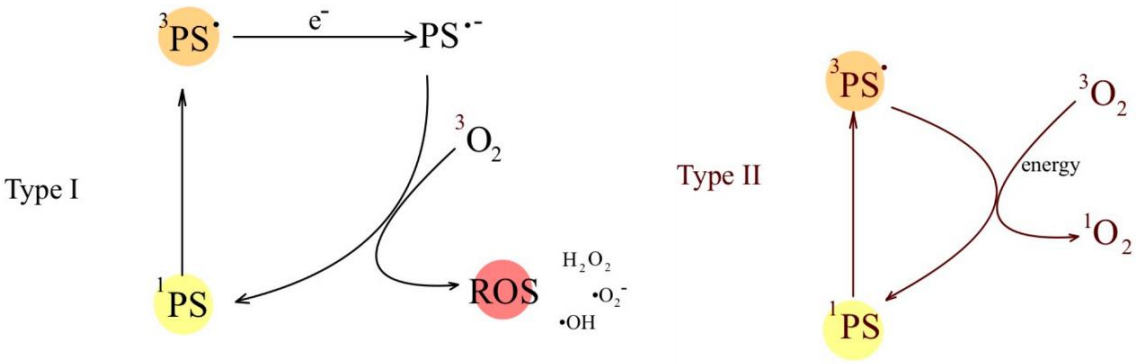

Figure 9. *schematic representation of Type 1 (on the right) and Type 2 (on the left) reaction mechanisms of PDT.*[27]

These locally generated reactive oxygen species (ROS) inflict severe oxidative damage that eradicates targeted tissue through three main interconnected mechanisms: direct cancer cell death via apoptosis or necrosis, indirect destruction by severely damaging the tumour-associated vasculature to cause localized hypoxia and starvation, and the stimulation of a robust anti-tumour immune response.[27]

The main advantage of PDT is its spatial selectivity, since ROS are generated only in the irradiated region containing the photosensitizer. This feature can limit damage to surrounding tissues and makes the treatment potentially repeatable and minimally invasive. Nevertheless, clinical translation of PDT remains limited not only by the dependence of the photodynamic process on oxygen availability, but also by choosing the right light wavelength. In fact, high-energy UV and visible radiation are strongly absorbed and scattered by biological chromophores, whereas longer wavelengths penetrate more deeply but may not provide sufficient energy to directly activate conventional photosensitizers or molecular oxygen. Therefore, PDT is limited by a trade-off between the improved tissue penetration of longer wavelengths and the energy required to activate the photosensitizer and generate cytotoxic ROS.[25,28] In addition, many molecular photosensitizers show poor aqueous solubility, limited stability under physiological conditions, and rapid systemic clearance, which can reduce their accumulation at the target site and affect their photodynamic efficiency.[1]

To overcome these limitations, nanotechnology has emerged as a promising pathway. In fact, nanoparticles (NPs) can improve the solubility and stability of hydrophobic photosensitizers, facilitate their delivery, and enable the integration of multiple optical or therapeutic functions within a single system.[1,2] The various investigated systems can be classified in organic and inorganic nanomaterials. The organic ones are mainly employed for their high biocompatibility and their ability to deliver photosensitizers and drugs, whereas inorganic nanomaterials are valued for their excellent optical properties, phototransduction capabilities, and high chemical stability.[1] A graphic representation of the main investigated NPs is reported in Figure 10.

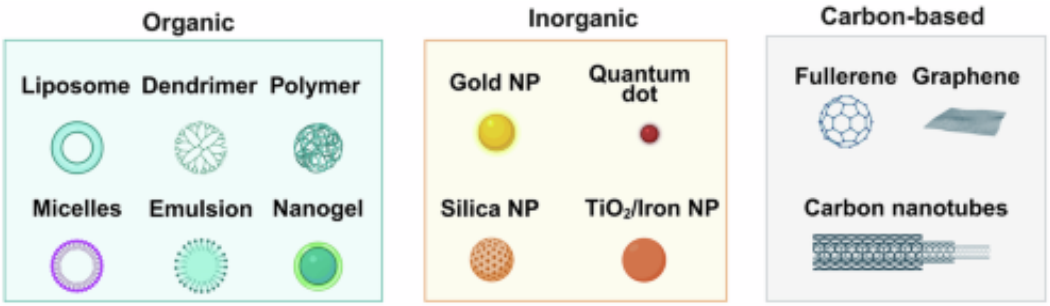

Figure 10. *Graphic representation of the main NPs systems with application in PDT.*[1]

Among the different nanotechnological approaches, lanthanide-doped upconversion nanoparticles have attracted considerable interest for PDT triggered by near-infrared (NIR) light, which lies precisely within the optical transparency window of biological tissues, where scattering and absorption by endogenous chromophores as well as phototoxicity from shorter wavelength are minimized. The resulting visible or ultraviolet emission can then be used to locally activate an associated photosensitizer or photoactive matrix.[2]

In this context, the material developed in this work is particularly relevant, as it is designed to operate under near-infrared (NIR) excitation and to generate reactive oxygen species through a synergistic combination of upconversion processes and TiO_2-based photocatalysis. The integration of a Yb^{3+}/Er^{3+} upconversion system with Ag-modified TiO_2 enables the conversion of 980 nm radiation into effective charge separation and ROS production, making the proposed nanoplatform a promising candidate for NIR-triggered PDT applications. Moreover, beyond the functional design of the system itself, an additional relevant aspect of the present work is the synthetic approach. The developed nanostructure is obtained through a fast and relatively simple one-pot strategy, which avoids the use of toxic or hazardous organic solvents, relying mainly on environmentally benign solvents such as water and propanol. This represents a significant advantage compared to many conventional multistep syntheses of functional nanomaterials, which often require harsh conditions, multiple purification steps, and the use of more problematic solvents. As a result, the proposed material not only provides a functional NIR-responsive nanoplatform for PDT, but also introduces a more sustainable synthetic route.

2. Materials and Methods

Chemicals purchased from Sigma Aldrich: Titanium (IV) isopropoxide (TTIP) 97% (CAS–No: 546–68–9); 2-Propanol (2-PrOH) ACS reagent ≥ 99,5% (CAS–No: 67–63–0); Silver nitrate ($AgNO_3$) ACS reagent ≥ 99.0% (CAS–No: 7761–88–8); Erbium (III) nitrate pentahydrate ($Er(NO_3)_3 \cdot 5H_2O$) 99,9% trace metals basis (CAS-No: 10031–51–3); Ytterbium (III) nitrate pentahydrate ($Yb(NO_3)_3 \cdot 5H_2O$) 99,9% metal basis (CAS–No: 35725–34–9); Ammonium nitrate ≥ 99.0% (NH_4NO_3) (CAS–No: 6484–52–2); 1,3-Diphenylisobenzofuran (DPBF) 97% (CAS–No: 5471–63–6).
Chemicals purchased from Carlo Erba reagents: Ammonium chloride (NH_4Cl) for analysis – ACS reagent (CAS–No: 12125–02–9).
Chemicals purchased from Thermo Fisher Scientific: Acetonitrile ≥ 99.9% HPLC gradient grade (CAS–No: 75–05–8),

2.1 Synthesis of Ag-, Er-, Tm-, Yb- doped TiO_2

TiO_2-based samples, including mono-doped Er-, and Yb- , as well as co-doped Er/Yb or materials, either with or without Ag modification, were synthesized via a sol-gel route adapted from the procedure reported by M. Santos et al.[29], followed by two different post-synthetic treatments, named Method 1 and Method 2.

Method 1: Washed. To obtain the undoped TiO_2 3.5 mL (11,8 mmol) of TTIP and 3.5 mL of 2-PrOH were mixed in a glass vial, followed by sonication for 15 minutes. Then, 8 mL of Milli-Q® water were added in a single portion, and the mixture was sonicated for an additional 15 minutes. The resulting gel was firstly washed with Milli-Q® water and 2-PrOH to remove unreacted reagents and then dried overnight at 80 °C in an oven. The dried material was then calcined in a tubular furnace at 450°C for 4h in air (100 mL/min) with a heating ramp of 2°C/min.
The same procedure was used to obtain the doped samples listed in Table 1 with the appropriate dopant precursors dissolved in the 8 mL of Milli-Q® water prior to its addition to the TTIP/2-PrOH mixture. The precursor amounts used were: 52.3 mg (0.118 mmol) of $Er(NO_3)_3 \cdot 5H_2O$, 530.0 mg (1.18 mmol) of $Yb(NO_3)_3 \cdot 5H_2O$, 78.3 mg (0.46 mmol) of $AgNO_3$.

Method 2: Unwashed. To better understand the effects of the washing treatment a second batch of samples was prepared following the same procedure described for Method 1.

The only difference was avoiding the washing step. After the sonication, the gel was transferred in the oven without any washing step and dried overnight at 80 °C before calcination under the same conditions reported before.

The acronyms of the synthesized samples, the dopant loadings and the corresponding preparation method are summarized in Table 1.

***Table 1**. Summary of the sample acronyms, the dopant loading and the corresponding preparation method. *The number at the end of each sample acronym (1 or 2) indicates the synthetic route used (Method 1 or Method 2, respectively). **The dopant loading is expressed as mol% relative to Ti (for example,* $1\ mol\%\ of\ Er = \frac{0.118\ mmol\ of\ Er}{11.8\ mmol\ of\ Ti} \times 100$*).*

	Dopant loading (mol%)				
Acronyms	**Ag**	**Er**	**Tm**	**Yb**	**Post-Synthetic treatment**
TiO_2_1	-	-	-	-	Method 1
TiO_2_Er_2	-	1	-	-	Method 2
TiO_2_Tm_1	-	-	1	-	Method 1
TiO_2_Tm_2	-	-	1	-	Method 2
TiO_2_Yb_2	-	-	-	10	Method 2
TiO_2_Ag_1	4	-	-	-	Method 1
TiO_2_Ag_2	4	-	-	-	Method 2
TiO_2_Er_Yb_1	-	1	-	10	Method 1
TiO_2_Er_Yb_2	-	1	-	10	Method 2
TiO_2_Er_Yb_Ag_1	4	1	-	10	Method 1
TiO_2_Er_Yb_Ag_2	4	1	-	10	Method 2

All the samples that included Ag modification showed a change in colour after calcination, from pure white to yellowish. Figure 11 reports photographs taken before and after calcination of the samples TiO_2_Er_Yb_Ag_1 and TiO_2_Er_Yb_Ag_2. It is

noticeable that the unwashed sample exhibits a more intense yellow coloration compared to the washed sample. This observation will be further discussed in the following sections.

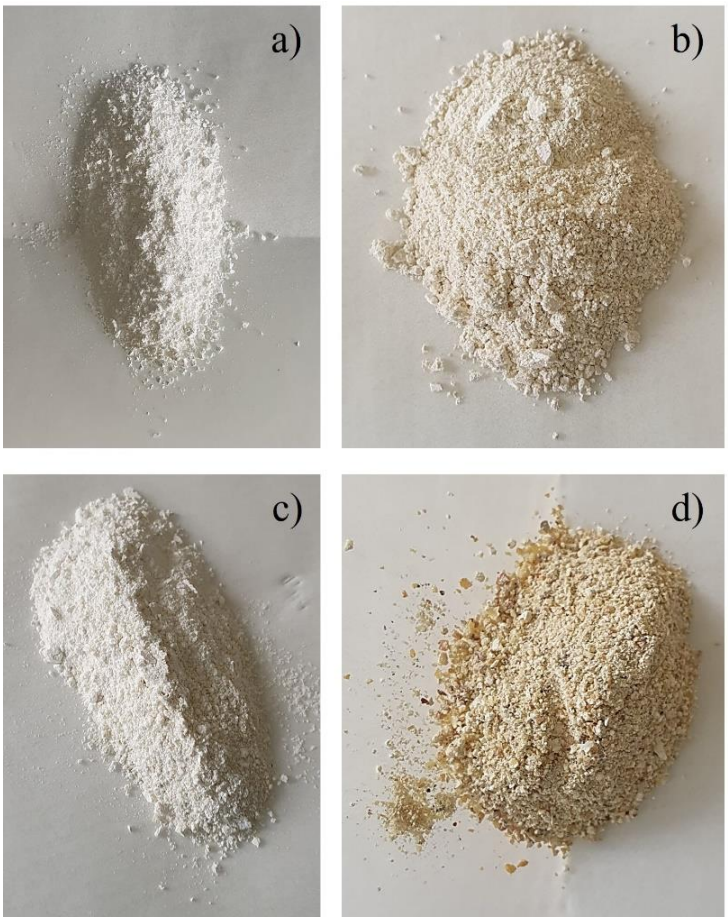

Figure 11. *Photographs of the samples before and after calcination: a) TiO_2_Er_Yb_Ag_1 before calcination; b) TiO_2_Er_Yb_Ag_1 after calcination; c) TiO_2_Er_Yb_Ag_2 before calcination; d) TiO_2_Er_Yb_Ag_2 after calcination.*

2.3 Physico-chemical Characterization

- X-ray powder diffractograms (XRPD) were collected on powder samples on a Bruker D8 Advance powder diffractometer (Karlsruhe, Germany), operating in Bragg–Brentano geometry, with a Cu anode target (used as an X ray source) equipped with a Ni filter and with a Linxeye XE-T high-resolution position sensitive detector. Trio and twin/twin optics are equipped on the DaVinci design modular XRD system. The X-ray tube of the instrument operates with Cu-Kα1 monochromatic radiation (λ = 1.54062 Å), with the current intensity and operative electric potential difference set to 40 mA and 40 kV, respectively, and with

automatic variable primary divergent slits and primary Soller slits of 2.5°. The X-ray profiles were recorded at room temperature in the 10°–90° 2ϑ with a coupled 2 ϑ – ϑ method, continuous PSD fast scan mode, time per step (rate or scan speed) of 0.100 s per step, and 2 ϑ step size (or increment) of 0.020°, with automatic synchronization of the air scatter (or anti scatter) knife and slits and with a fixed illumination sample set at 17 mm.

- Elemental composition (Ti, Ag, Er, Yb) was determined by energy dispersive X-ray fluorescence spectroscopy (ED-XRF), using a Rigaku NEX CG II series 3D cartesian geometry ED-XRF spectrometer (Tokyo, Japan) operating with a high-power X-ray tube (50 kV−50 W/65 kV−100 W) and a large-area high-throughput silicon drift detector (SDD), analyzing Na to U elements. The instrument is equipped with a vacuum/helium purge, automatic sample changers and a sample spinner tray. Samples were measured at solid state using dedicated 32 mm double open-ended samples cups equipped with ring and cap, with a 4 mm Mylar® (PP) thin film.
- Field emission scanning electron microscopy (FE-SEM) images were acquired on a Gemini SEM 360 scanning electron microscope (Zeiss, Oberkochen, Germany) equipped with a Schottky-type field effect emitter as the electron source. Before the analysis, to prevent the insulating particles from becoming electronically charged under the electron beam, a conductive coating of platinum (12,66 nm) was deposited on the samples by chemical vapor deposition (CVD) using the Desk Sputter Coater DSCT1-F (Vac Coat, Golders Green, London, UK.). The samples were prepared depositing a few drops of the material previously dispersed in water and filtered with a 0.45 μm filter onto an aluminium stub coated with conductive carbon tape. For transmission electron imaging, a multi-mode Scanning Transmission Electron Microscopy (STEM) detector (aSTEM) integrated into the ZEISS GeminiSEM 360 platform was utilized. Samples were deposited onto carbon-coated copper TEM grids and mounted onto a dedicated STEM holder.
- Dynamic light scattering (DLS) analysis was carried out in aqueous solution by using a Malvern Zetasizer NanoZS instrument (Malvern Panalytical, Grovewood Road, UK) equipped with a He-Ne laser (λ = 633 nm). The DLS measurements were performed at neutral pH and 25 °C. The sample suspensions were prepared by dispersing 3 mg of solid compound in 30 mL of ultrapure water and sonicating

at 59 kHz for 15 min. The dispersion was measured both before and after filtration with a 0.45 μm filter.

- Diffuse reflectance UV-Vis-NIR (DR UV-Vis-NIR) spectra were collected on pure solid samples with a PerkinElmer LAMBDA 900 UV-Vis-NIR double-beam spectrophotometer (Waltham, MA, USA) in the range of 200–2000 nm, with a resolution of 1 nm.
- The Er^{3+}/Yb^{3+} upconversion (UC) process was investigated by collecting emission spectra on a Horiba Jobin-Yvon Model IBH FL-322 Fluorolog 3 Spectrometer (Northampton, UK) equipped with a 450 W Xenon arc lamp, double grating excitation and emission monochromators (2.1 $nm \cdot mm^{-1}$ dispersion; 1200 grooves per mm), a Hamamatsu Model R928 photomultiplier tube and a PSU–III–LED 980 nm laser. The emission UC spectra were collected in the range of 500–700 nm using a laser power of 1240 mW (1430 mA).
- Photoluminescence (PL) measurements were performed by using an Edinburgh FLSP920 spectrophotometer equipped with a Hamamatsu R928P PMT detector (200–900 nm) and a Hamamatsu R5509-72 NIR PMT detector (500–1700 nm). Steady-state PL spectra were acquired illuminating the sample with a 450 W continuous-wave (CW) xenon lamp. Appropriate optical filters were used, and steady-state emission data were corrected for the instrumental spectral response. All PL measurements were recorded at room temperature. Solid-state samples were put between quartz plates (Starna cuvette type 20/C/Q/0.2).

2.4 Reactive oxygen species generation

To evaluate the ability of the samples to generate reactive oxygen species (ROS), such as singlet oxygen ($^1O_2$), 1,3-Diphenylisobenzofuran (DPBF) was used as a probe in the following procedure:

3,5 mL of acetonitrile, 87,5 μL of a 1×10^{-3} M stock solution of DPBF in acetonitrile and 0,5 mg of the selected sample were added to a quartz cuvette. Then, UV-Vis spectra were collected after different irradiation times (from 0 to 60 min) using two different excitation wavelengths:

- 980 nm, using the laser, corresponding primarily to the absorption band of Yb^{3+} ions, to evaluate the ability of the material to generate ROS species through upconversion;

- 522 nm, using a Xenon lamp, corresponding to the main green emission band of Er^{3+}, to assess the possibility of energy transfer between Er^{3+} and TiO_2 .

As a reference the same procedure was carried out without the addition of the solid sample.

All the UV-Vis absorption spectra were recorded at 25 °C in the 250–800 nm range with a resolution of 1 nm using a double-beam PerkinElmer LAMBDA 1050+ UV-Vis-NIR Spectrophotometer (Waltham, MA, USA).

3. Results and discussion

The goal of this research activity is the synthesis of TiO_2 nanoparticles (NPs) able to generate reactive oxygen species (ROS) species under near-infrared (NIR) irradiation by exploiting NIR to visible upconversion processes with potential applications in photodynamic therapy (PDT). A series of TiO_2-based materials, including mono-doped (Er-, Tm-, and Yb-) and co-doped (Er/Yb and Tm/Yb) samples, with and without Ag modification, were synthesized and systematically characterized. Particular attention was devoted to evaluating the influence of the dopant in the titania matrix, silver incorporation, and post-synthetic treatment on the structural, morphological, and optical properties of the obtained materials. Furthermore, the effects of the two synthetic protocols (Method 1 and Method 2) were investigated to identify the most suitable conditions for enhancing the upconversion-assisted photocatalytic activity and ROS generation under NIR excitation. To achieve these information a multi-technique approach was used combining the following characterization techniques: X-Ray powder diffraction (XRPD), X-Ray fluorescence spectroscopy (XRF), Field emission scanning electron microscopy (FE-SEM), Scanning transmission electron microscopy (STEM), Dynamic light scattering (DLS), Diffuse reflectance UV-Vis spectroscopy (DR UV-Vis) and Photoluminescence (PL) spectroscopy.

3.1 Ag-, Er-, Tm-, Yb- doped TiO_2

3.1.1 X-Ray powder diffraction (XRPD)

XRPD was employed to investigate the crystalline structure of the synthesized NPs upon calcination at 450°C. In particular, the analysis was performed to identify the predominant TiO_2 crystalline phase (anatase, rutile, brookite, or monoclinic), to evaluate whether the incorporation of the dopants induced any structural modifications in the TiO_2 lattice and assess the influence of the two post-synthetic treatments on the resulting crystalline structure.

Figure 12 illustrates the XRPD pattern of the pristine TiO_2_1 nanoparticles (NPs). It exhibits diffraction peaks at 2ϑ = 25.28, 37.80, 48.05, 50.06, 62.69, 68.76, 70.31, 75.03, 82.66 which corresponds, respectively, to the (101), (004), (200), (211), (204), (116), (220), (215), (224) of the tetragonal anatase TiO_2 phase. [36–39] This information is in good agreement with the Joint Committee on Powder Diffraction Standards (JCPDS) card No.

21-1272. A weak diffraction peak at 2θ = 30.8° was also detected and assigned to the (121) plane of brookite TiO_2, indicating the presence of a minor brookite fraction.[38] These results suggest that the simple and fast sol-gel synthesis procedure used in this work leads primarily to the formation of anatase phase along with minor brookite phase. This information aligns with literature that shows that the formation of anatase phase occurs at temperatures below 600°C.[37] Therefore, a calcination temperature of 450°C was selected for the present study. Among the various TiO_2 polymorphs, anatase is widely recognized as the most photocatalytically active phase thanks to its band bending property which enhances surface hole trapping, thereby promoting the generation of free radicals and making it particularly attractive for PDT applications.[8]

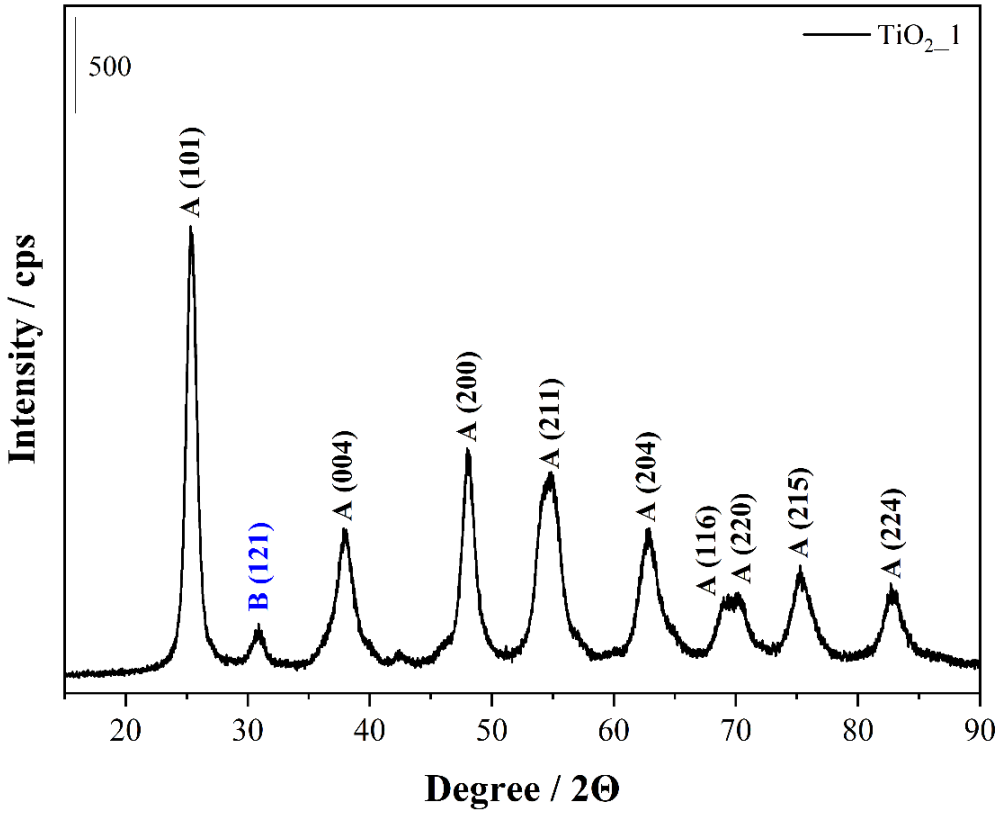

Figure 12. *XRPD pattern of the TiO_2_1 NPs, with the diffraction peaks indexed according to their corresponding crystallographic planes. *A=anatase, B=brookite*

Figure 13 (a-c) compares the XRPD patterns of all synthesized TiO_2-doped NPs. All materials exhibit the same diffraction pattern observed for the TiO_2_1 NPs shown in Figure 12. The diffraction reflections can be assigned predominantly to the anatase phase, with a minor contribution from brookite. These results demonstrate that the incorporation of Er^{3+}, Yb^{3+}, and Ag dopants does not alter the crystal structure of TiO_2 under the adopted synthesis conditions. Moreover, the lack of additional peaks associated with crystalline

phases of the dopant species, suggest a homogeneous dispersion of the dopants within anatase crystallites.[29,40]

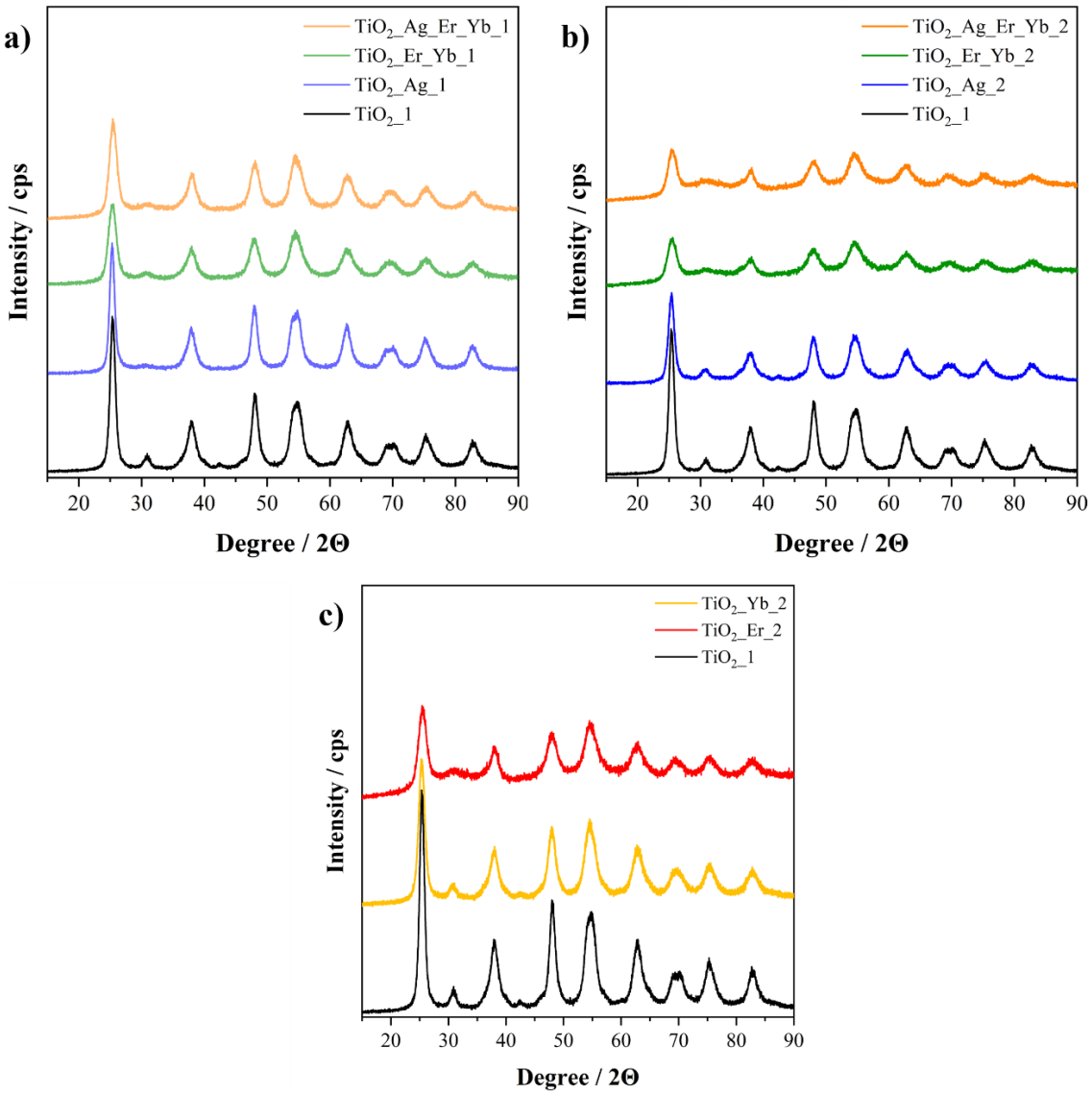

Figure 13. *Comparison of the XRPD patterns of all synthesized TiO_2-doped NPs. a) Washed samples (Method 1); b) Unwashed samples (Method 2); c) mono-doped samples.*

Figure 14 (a-c) highlights the effect of the two post-synthetic treatments on the crystal structure of the synthesized NPs. As observed in Figure 12, all samples exhibit the characteristic reflections of anatase TiO_2 together with a minor brookite contribution, indicating that the washing treatment does not affect the crystalline phase composition. However, the doped NPs display broader and less intense reflections compared to undoped TiO_2, particularly in the unwashed series. This observation suggests that dopant

incorporation may hinder crystal growth and slightly reduce the crystallinity of the nanomaterials.[41]

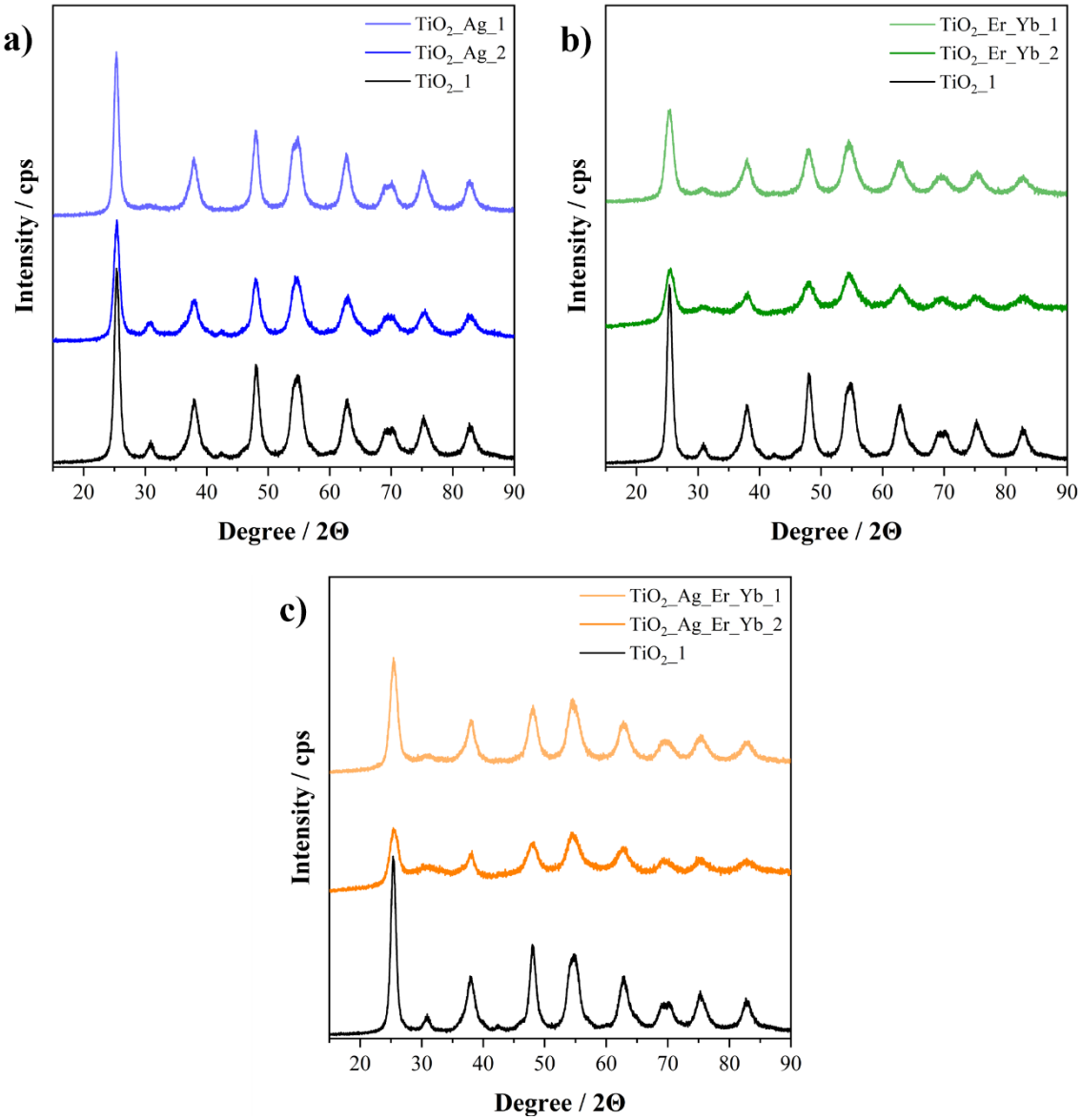

Figure 14. *Comparison of the effect of the post-synthetic treatments on the crystal structure. a) TiO_2_Ag_1 vs TiO2_Ag_2 samples; b) TiO_2_Er_Yb_1 vs TiO_2_Er_Yb_2 samples; c) TiO_2_Ag_Er_Yb_1 vs TiO_2_Ag_Er_Yb_2 samples*

In conclusion, the collected XRPD analysis demonstrates that all the synthesized NPs are composed primarily of anatase phase, with only a minor contribution from brookite. Neither dopant incorporation nor the washing treatment affected the crystalline phase composition of TiO_2. However, the presence of the dopants resulted in a slight decrease in crystallinity, as evidenced by the broadening and attenuation of the diffraction reflections. This effect was particularly evident in the unwashed samples.

3.1.2 X-Ray fluorescence spectroscopy (XRF)

Several studies have shown that the optimal Ag loading to effectively enhance the visible-light photocatalytic activity of TiO_2 is between 4 and 5 mol%. Lower Ag concentrations do not produce significant improvements, whereas at higher Ag contents, Ag metal nanoparticles tend to aggregate, forming larger particles that lead to a decrease in the photocatalytic performance.[29,42–44] The Er^{3+} and Yb^{3+} concentrations were selected according to previous investigation conducted by our research group on rare earth doped TiO_2 materials. In this systems Yb^{3+} acts as the sensitizer and is therefore typically employed at a significantly higher concentration than the activator (Er^{3+}) to maximize the absorption of 980 nm radiation and promote efficient energy transfer.[15,16,45]

On the basis of these considerations, nominal dopant loadings of 4 mol% for Ag, 1 mol% for Er^{3+}, and 10 mol% for Yb^{3+} were selected. The actual elemental composition of the synthesized samples was subsequently assessed by XRF analysis to verify its agreement with the nominal values. The results of the XRF analysis are reported in Table 3. NPs prepared without the washing treatment (Method 2) exhibit dopant concentrations very close to the nominal values. In contrast, the washed NPs (Method 1) show significantly lower dopant contents, indicating that the washing step leads to a partial loss of the dopant precursors and, consequently, to a lower final dopant concentration. This observation is consistent with the visual appearance of the samples shown in Figure 1. In particular, the unwashed Ag-containing samples display a more intense yellow coloration than the corresponding washed samples. Since yellow coloration has previously been associated with Ag incorporation into TiO_2[29,42–44,46,47], this qualitative observation further supports the higher Ag content determined by XRF.

These findings are also consistent with the XRPD patterns reported in Figure 4(a-c). As previously reported, the doped NPs exhibited broader and less intense diffraction peaks, particularly in the unwashed series, indicating a lower degree of crystallinity. The higher dopant concentrations determined by XRF for these samples further support the hypothesis that dopant incorporation reduces the crystallinity of TiO_2. Moreover, the comparison between washed and unwashed samples suggests that this effect becomes

more pronounced as the dopant concentration increases, indicating a correlation between dopant loading and the extent of crystallinity loss.

Table 2. *Elemental composition of the synthesized samples obtained by XRF analysis.*

Sample	**TiO_2 (mol%)**	**Ag (mol%)**	**Er (mol%)**	**Yb (mol%)**
TiO_2_1	100.000 ± 0.007	-	-	-
TiO_2_Er_2	98.90 ± 0.01	-	1.090 ± 0.006	-
TiO_2_Yb_2	90.10 ± 0.01	-	-	9.9 ± 0.2
TiO_2_Ag_1	97.600 ± 0.007	2.350 ± 0.001	-	-
TiO_2_Ag_2	96.200 ± 0.008	3.780 ± 0.002	-	-
TiO_2_Er_Yb_1	96.70 ± 0.01	-	0.283 ± 0.003	3.0 ± 0.2
TiO_2_Er_Yb_2	89.50 ± 0.01	-	0.911 ± 0.004	9.6 ± 0.2
TiO_2_Ag_Er_Yb_1	95.00 ± 0.01	2.140 ± 0.002	0.252 ± 0.003	2.7 ± 0.2
TiO_2_Ag_Er_Yb_2	87.00 ± 0.01	3.410 ± 0.002	0.825 ± 0.004	8.8 ± 0.2

Interestingly, despite the different absolute dopant concentrations, the experimental Yb/Er molar ratio remained remarkably close to the nominal value of 10 for all co-doped samples, as shown in Table 4. This indicates that the washing treatment affects both rare-earth dopants to a similar extent, preserving the sensitizer-to-activator ratio required for efficient upconversion.

Table 3. *Summary of the Yb/Er ratio of the Er^{3+}- Yb^{3+}-doped samples (with and without Ag).*

	TiO_2_Er_Yb_1	**TiO_2_Er_Yb_2**	**TiO_2_ Ag_Er_Yb_1**	**TiO_2_ Ag_Er_Yb_2**
Yb /Er	10.6 ± 0.7	10.5 ± 0.2	10.7 ± 0.8	10.7 ± 0.3

In conclusion, XRF analysis demonstrate that the washed samples contain significantly lower absolute amount of dopants than the unwashed samples, indicating that Method 2 is better in retaining the nominal dopant loading. Yb/Er ratio, however, is not influenced by the post-synthetic treatment and is maintained around 10 for all the co-doped samples which is an optimal value for upconversion applications.

3.1.3 Field Emission Scanning Electron Microscopy (FE-SEM) and Scanning Transmission Electron (STEM) Microscopy

To gain detailed insights into the morphological features, particle size, and aggregation state of the synthesized materials, Field Emission Scanning Electron Microscopy (FE-SEM) and Scanning Transmission Electron Microscopy (STEM) analyses were performed.

Figure 15 (a-b) reports the FE-SEM micrographs of the undoped TiO_2 sample at two different magnifications. The material displays a highly uniform, quasi-spherical morphology with a primary particle size visually estimated under 50 nm, though the highly agglomerated nature of the sample doesn't allow for a precise measurement of the NPs dimension, in this analysis conditions. This result is in good agreement with other works where a sol-gel method was employed to synthesise TiO_2 NPs. [29,42,46,47]

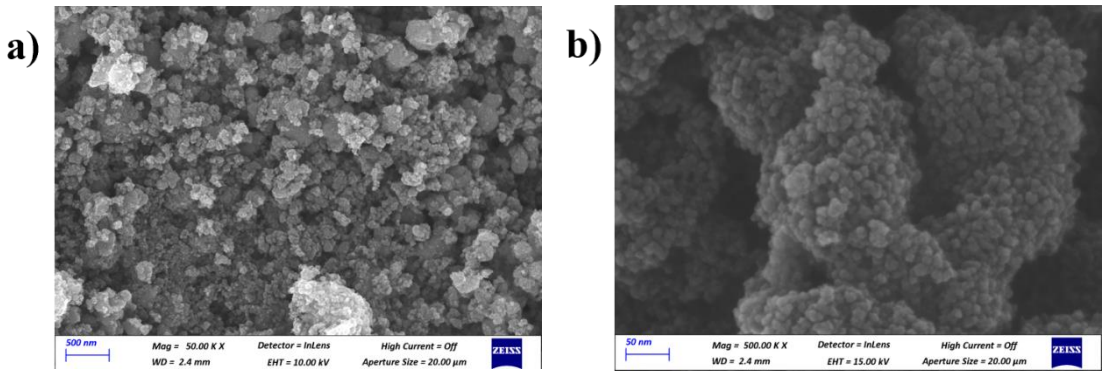

***Figure 15**. FE-SEM micrographs of TiO_2_1.*

Figure 16 (a-b) illustrates a high-magnification FE-SEM comparison at identical imaging conditions to evaluate the morphological impact of dopant introduction, specifically comparing TiO_2_Er_Yb_1 (a) and TiO_2_Ag_Er_Yb_1 (b).

Both materials preserve the primary spherical shape seen for TiO_2_1, suggesting that neither lanthanides nor Ag presence in the matrix affect the material morphology.

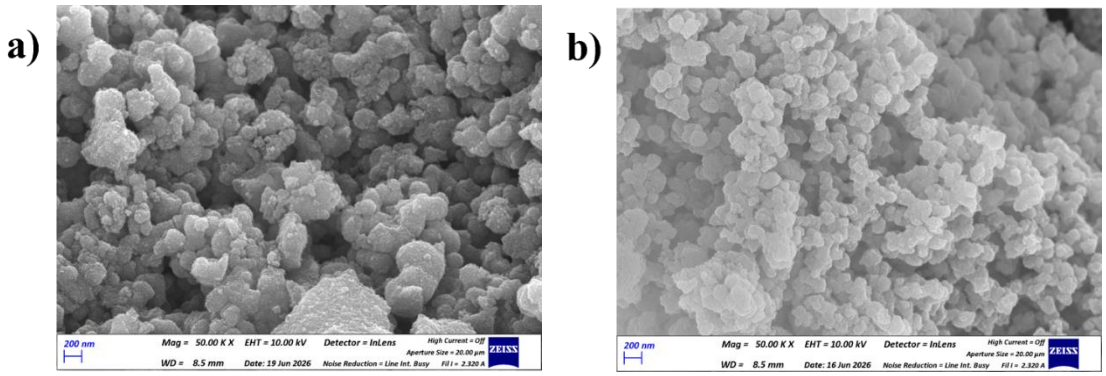

Figure 16. *FE-SEM micrographs of TiO_2_Er_Yb_1 (a) and TiO_2_Ag_Er_Yb_1 (b).*

To accurately resolve individual particle boundaries and investigate the nanostructure at a higher resolution, STEM imaging was performed on dispersed samples. Figure 17 (a-c) reports the micrographs, registered in the same conditions, of TiO_2_Er_Yb_1 (a) and TiO_2_Ag_Er_Yb_1 (b-c). Both samples shows spheric particles with dimensions well under 100 nm.

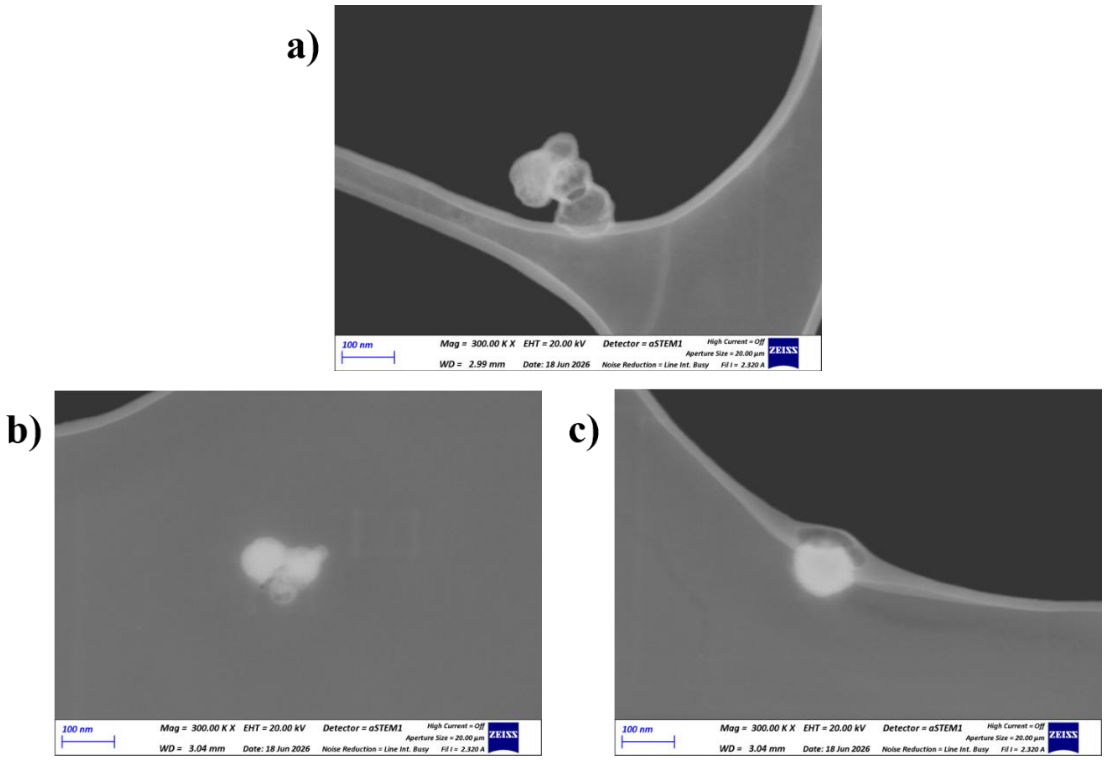

Figure 17. *STEM micrographs of TiO_2_Er_Yb_1 (a) and TiO_2_Ag_Er_Yb_1 (b-c).*

In conclusion, the combination of FE-SEM and STEM analysis provided insights into the samples morphology indicating a spheric particle shape and dimensions estimated between 50 to 100 nm. Moreover, the lanthanide doping and Ag incorporation doesn't seem to largely affect the sample morphology.

3.1.4 Dynamic light scattering

Dynamic light scattering (DLS) measurements were performed to further investigate the size of the TiO_2 nanoparticles and to compare it with the particle sizes observed by FE-SEM and STEM. In addition, DLS analysis provided information on the behaviour of the nanoparticles in water, including the possible presence of particle agglomerates. To this end, the samples were analysed both before and after filtration through a 0.45 µm filter in order to remove larger nanoparticles. The results obtained for TiO_2_1 and TiO_2_Ag_1 are reported in Figures 10 and 11, respectively.

Figure 18 (a-b) shows the DLS results obtained for the undoped TiO_2 sample in water. Before filtration (Figure 10a), two main peaks centred at approximately 81 nm and 291 nm are observed. The presence of two populations suggests that, besides smaller nanoparticles, larger agglomerates are also present in the aqueous dispersion. After filtration (Figure 18b), only one peak centred at approximately 97 nm is detected, while the signal associated with the larger population disappears. This result supports the attribution of the peak at around 291 nm to agglomerated particles, which were removed by filtration.

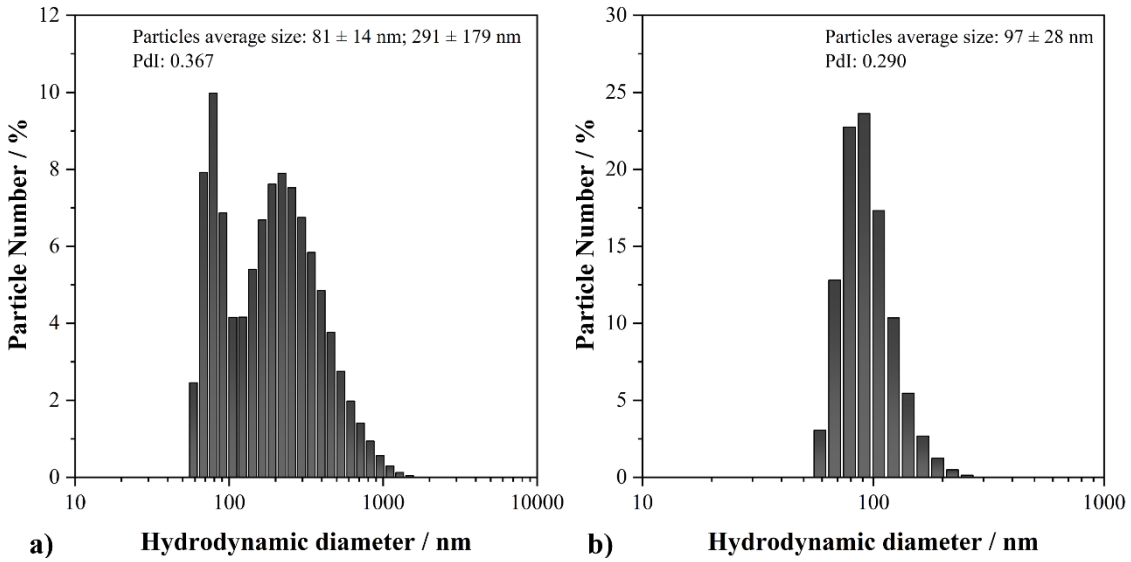

***Figure 18**. DLS histograms of (a) unfiltered TiO_2_1 and (b) filtered (0.45 µm) TiO_2_1.*

Figure 19 (a-b) reports the DLS results of the TiO_2_Ag_1 sample. Before filtration (Figure 19a), two main populations centred at approximately 185 nm and 656 nm are observed, indicating the coexistence of smaller particles or aggregates and larger agglomerates in the aqueous dispersion. After filtration (Figure 19b), the peak associated with the larger population disappears, while a single broad distribution centred at approximately 495 nm

is detected. This result suggests that filtration removes the largest agglomerates; however, the remaining particles are still characterized by a relatively large hydrodynamic diameter. Compared with TiO_2_1, TiO_2_Ag_1 shows larger hydrodynamic dimensions both before and after filtration. This behaviour may be related to the presence of Ag-clusters on the surface of the TiO_2 NPs, that form after calcination.

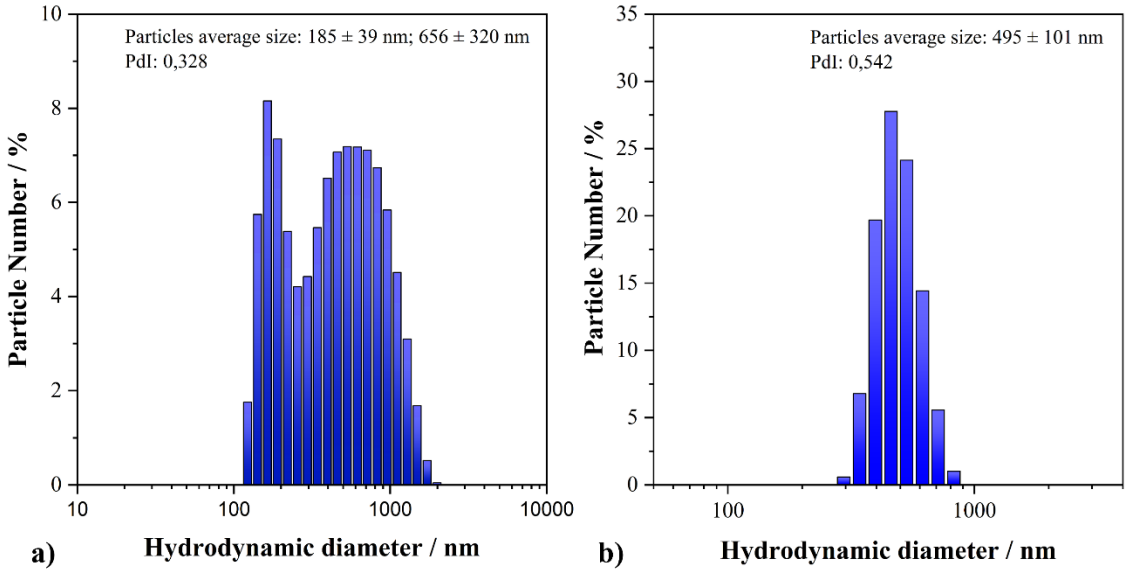

Figure 19. *DLS histograms of (a) unfiltered TiO_2_Ag_1 and (b) filtered (0.45 µm) TiO_2_Ag_1.*

In conclusion, the DLS analysis provides a confirmation informations evidenced by FE-SEM and TEM analysis. In fact, the visual estimation obtained from the microscopic images indicated a spherical particle shape with dimensions positioned between 50 to 100 nm. When dispersed in water, the undoped TiO_2 sample exhibits a population centred at around 81 nm, which is in perfect agreement with the nanoparticle dimensions observed under the microscope. However, the presence of the second larger peak at approximately 291 nm directly reflects the highly agglomerated nature of the sample, which was already noted during the FE-SEM analysis. The fact that filtration successfully removes this larger population indicates that these macro-aggregates are composed of the smaller 50–100 nm spherical particles.

3.1.5 Diffuse reflectance UV-Vis-NIR spectroscopy (DR UV-Vis-NIR)

DR UV-Vis-NIR analysis were performed to investigate the optical absorption properties of the synthesized NPs. Specifically, this analysis aimed to: (i) confirm the successful incorporation of Er^{3+}, and Yb^{3+} in TiO_2 network through the identification of their

characteristic absorption bands; (ii) evaluate the effect of Ag introduction on the TiO_2 band gap and assess whether it broadens the absorption toward the Vis region, thereby improving the spectral overlap with the Er^{3+} absorption bands and potentially enhancing the energy transfer responsible for ROS generation; and (iii) provide additional evidence of the different dopant concentrations observed by XRF, since samples with lower dopant contents are expected to exhibit correspondingly weaker rare-earth absorption features.[48]
All DR UV-Vis spectra exhibit a broad absorption band between 200 and 400 nm, corresponding to the TiO2 band gap.[29,47]
DR UV-Vis spectra of undoped TiO_2 together with the mono-doped Er^{3+}- and Yb^{3+}-samples and the co-doped Er^{3+}/Yb^{3+} materials, both with and without Ag-doping, are reported in Figure 20. The spectra of TiO_2_Er_2 (in yellow) and TiO_2_Yb_2 (in red) allow the identification of the characteristic absorption features of Er^{3+} and Yb^{3+}, respectively. In the TiO_2_Er_2 spectra, the narrow absorption bands observed in the visible region arise from the intra-4f electronic transitions of Er^{3+} and can be assigned to the following transitions peaks:

- 450 nm: $^4I_{15/2} \rightarrow {}^4F_{5/2}$
- 488 nm: $^4I_{15/2} \rightarrow {}^4F_{7/2}$
- 520 nm: $^4I_{15/2} \rightarrow {}^2H_{11/2}$
- 543 nm: $^4I_{15/2} \rightarrow {}^4S_{3/2}$
- 653 nm: $^4I_{15/2} \rightarrow {}^4F_{9/2}$

An additional band is observed at 975 nm corresponding to the $^4I_{15/2} \rightarrow {}^4I_{11/2}$ transition of Er^{3+}.
On the other hand, the TiO_2_Yb_2 spectra exhibits a broader absorption peak with a maximum at 975 nm that corresponds to the $^2F_{7/2} \rightarrow {}^2F_{5/2}$ transition.[48–50]
In the co-doped Er^{3+}/Yb^{3+} samples, all these characteristic absorption bands are observed, confirming presence of both rare-earth ions in the TiO_2 NPs. Furthermore, neither Ag doping nor the post-synthetic washing treatment alters the characteristic absorption features of Er^{3+} and Yb^{3+} ions, indicating that both modifications preserve the optical properties of the rare-earth dopants.

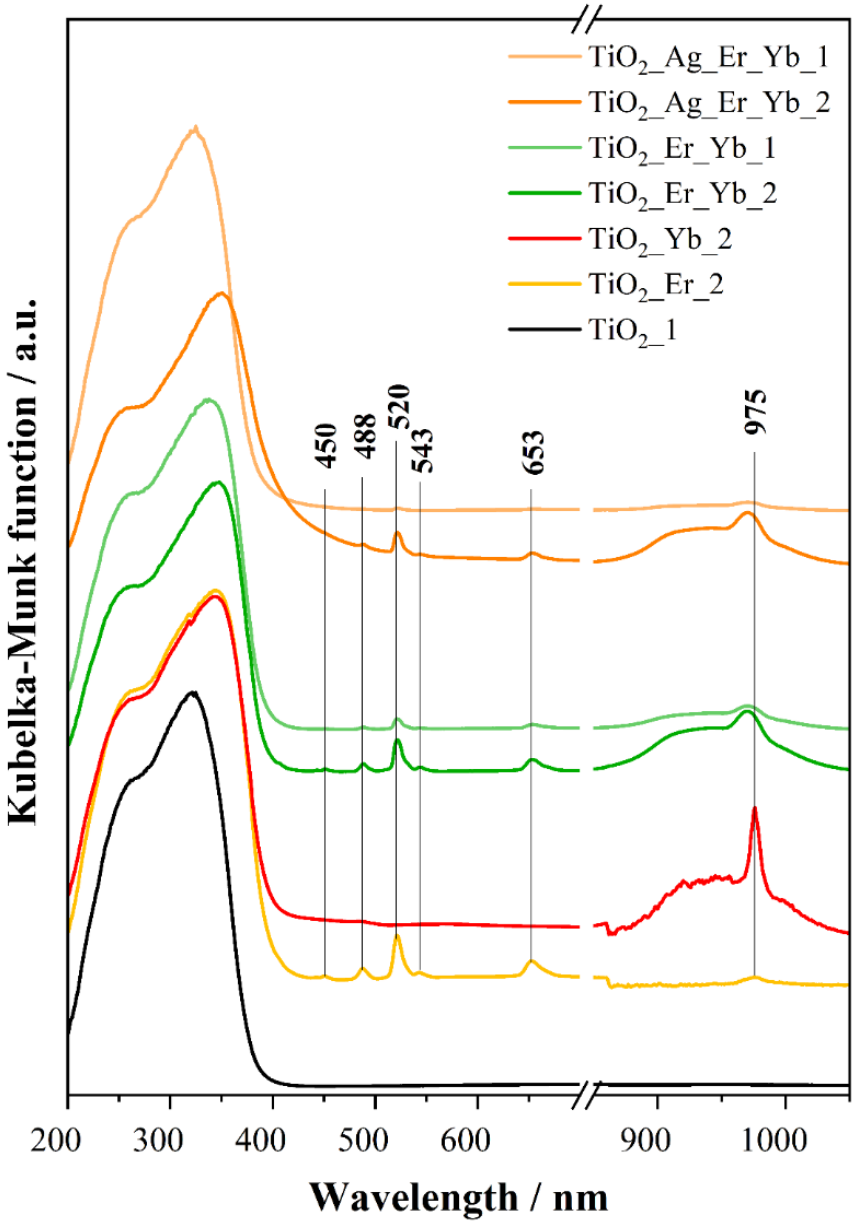

Figure 20. *DR UV-Vis-NIR spectra of undoped TiO_2, mono-doped Er^{3+}- Yb^{3+}- TiO_2 and co-doped Er^{3+}/Yb^{3+} TiO_2 both with and without Ag.*

A comparison between DR UV-Vis-NIR spectra of TiO_2_Er_Yb_1, TiO_2_Er_Yb_2 and undoped TiO_2 is reported in Figure 21. It is noticeable that the doped samples show a slight shift of the absorption maximum of TiO_2, especially the unwashed ones. The unwashed samples contain higher dopant concentrations, suggesting that the increased dopant incorporation, as evidenced by XRF results, slightly affect the TiO_2 band gap.[48] Moreover, TiO_2_Er_Yb_2 exhibits significantly more intense Er^{3+} and Yb^{3+} absorption bands than TiO_2_Er_Yb_1. Since the intensity of the rare-earth absorption bands is proportional to the dopant loadings,[48,50] this observation is fully consistent with the XRF

analysis and further confirms that Method 2 is more effective at retaining the nominal dopant loading than Method 1.

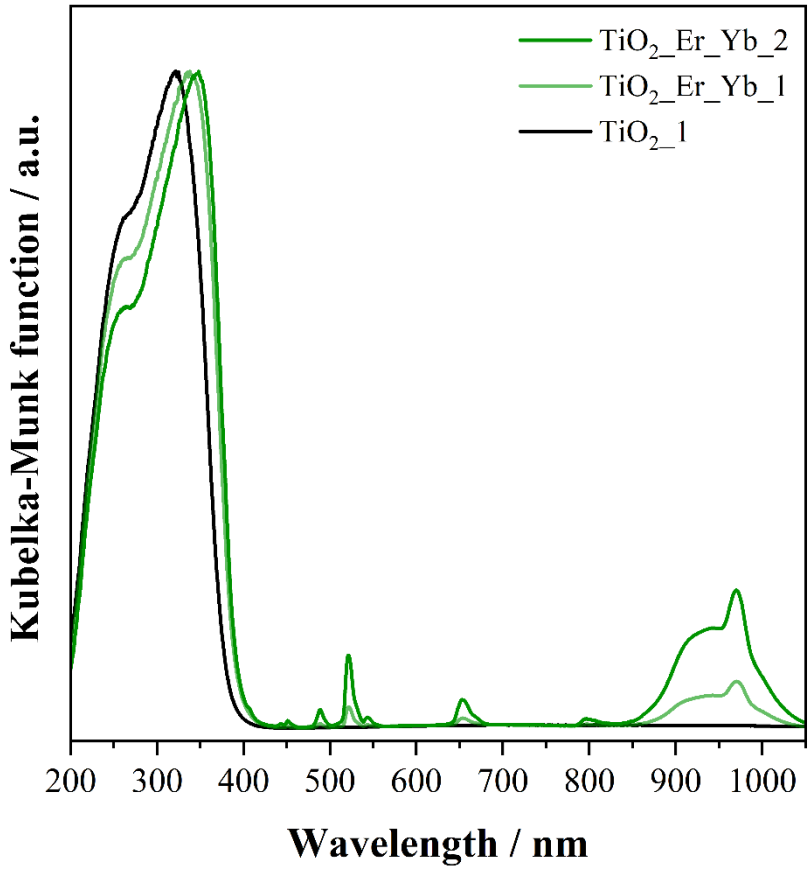

Figure 21. *Comparison between the DR UV-Vis-NIR spectra of TiO_2_Er_Yb_1, TiO_2_Er_Yb_2 and undoped TiO_2. *The spectra have been normalized between 0 and 1.*

DR UV-Vis-NIR spectra of TiO_2_Ag_1 and TiO_2_Ag_2 in comparison to the undoped TiO_2 are reported in Figure 22. Both Ag-doped samples exhibit a red shift of the TiO_2 absorption edge compared with undoped TiO_2 NPs. The shift is more pronounced for the unwashed sample (TiO_2_Ag_2), which is to be expected considering the higher Ag content determined by XRF. The observed red shift is consistent with previous reports on Ag-modified TiO_2, where silver incorporation has been shown to alter the electronic structure of the semiconductor, leading to an apparent narrowing of the optical band gap and an extension of the absorption toward the visible region. During calcination treatment, Ag^+ ions are not expected to substitute Ti^{4+} within the anatase lattice because of their considerably larger ionic radius. Instead, they tend to migrate toward the nanoparticle surface, where metallic Ag clusters are formed. These surface Ag clusters establish a metal–semiconductor interface with TiO_2, promoting electron transfer from the TiO_2 conduction band to Ag and resulting in the formation of a Schottky barrier. This

interface acts as an efficient electron sink, suppressing electron–hole recombination and thereby enhancing the photocatalytic activity. Residual Ag^{+} species may also contribute by acting as electron trapping centres.[44]

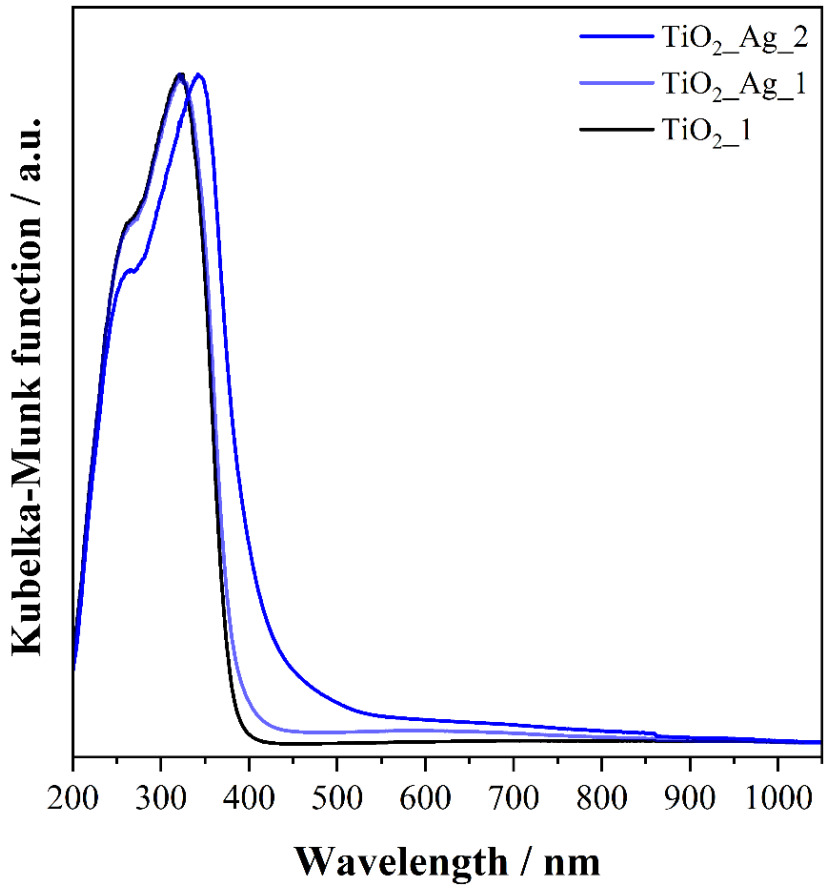

Figure 22. *Comparison between the DR UV-Vis-NIR spectra of TiO_2_Ag_1, TiO_2_Ag_2 and undoped TiO_2. *The spectra have been normalized between 0 and 1.*

Figure 23 compares the DR UV-Vis-NIR spectra of undoped TiO_2, TiO_2_Ag_Er_Yb_1 and TiO_2_Ag_Er_Yb_2. As previously discussed, all samples exhibit the broad absorption band associated with the TiO_2 band gap together with the characteristic absorption bands of Er^{3+} and Yb^{3+}. The spectra further demonstrate that Ag incorporation broadens the TiO_2 absorption edge toward the visible region even in the presence of the rare-earth dopants.

Furthermore, TiO_2_Ag_Er_Yb_2 exhibits not only more intense Er^{3+} and Yb^{3+} absorption bands than TiO_2_Ag_Er_Yb_1, but also a more pronounced red shift of the TiO_2 absorption edge. These observations are fully consistent with the XRF results and with the behaviour observed for the Ag-doped samples (Figure 22), indicating that the higher dopant concentration retained in the unwashed material enhances both the rare-earth absorption features and the Ag-induced modification of the TiO_2 optical response.

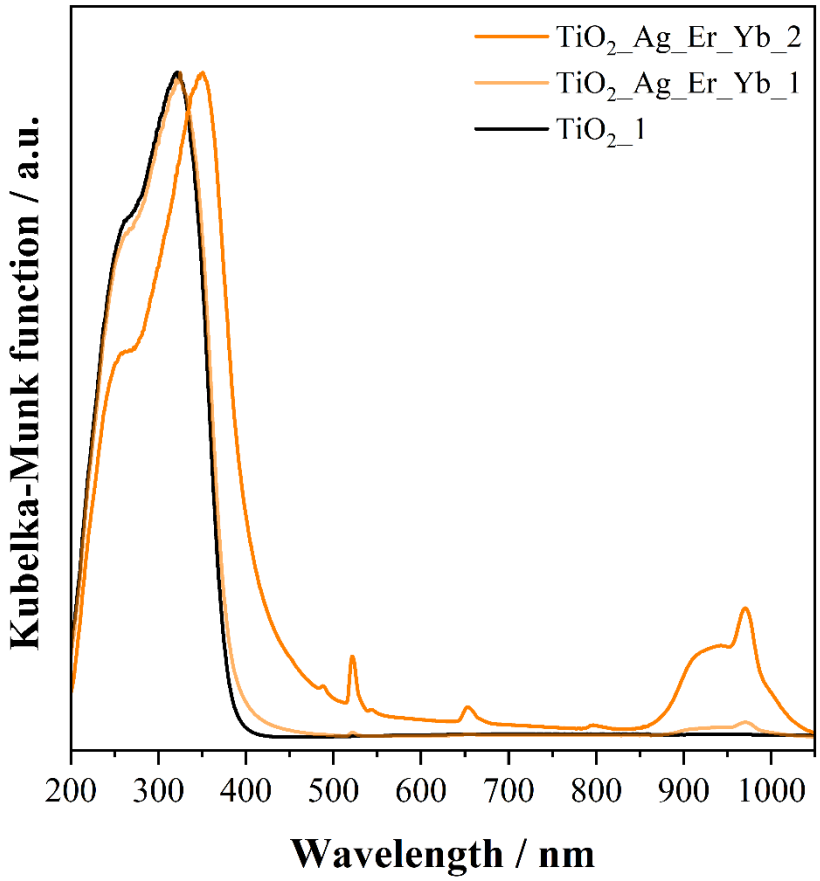

Figure 23. *Comparison between the DR UV-Vis-NIR spectra of TiO_2_Ag_Er_Yb_1, TiO_2_Ag_Er_Yb_2 and undoped TiO_2. *The spectra have been normalized between 0 and 1.*

Finally, Figure 24 provides an immediate comparison between the samples prepared by Method 1 (a) and the samples prepared by Method 2 (b), with the undoped TiO_2 spectra included as reference. The DR UV–Vis–NIR analysis confirms both the characteristic optical response of TiO_2 and the successful incorporation of Er^{3+} and Yb^{3+} in the mono- and co-doped materials through the observation of their characteristic absorption bands. Ag modification resulted in a significant red shift of the TiO_2 band gap, and this behaviour was maintained also in the Ag- Er^{3+}- Yb^{3+}- co-doped samples, indicating that Ag preserves its ability to extend the optical absorption of TiO_2 toward the visible region even in the presence of Er^{3+} and Yb^{3+}, while the rare-earth ions retain their characteristic absorption bands. This confirms that the simultaneous incorporation of Ag and lanthanides does not compromise the optical features contributed by each dopant. A comparison between the two post-synthetic treatments further reveals that the unwashed samples consistently exhibit more intense Er^{3+} and Yb^{3+} absorption bands than their washed counterparts. This

observation is in excellent agreement with the XRF results, confirming that Method 2 retains a higher dopant loading than Method 1.

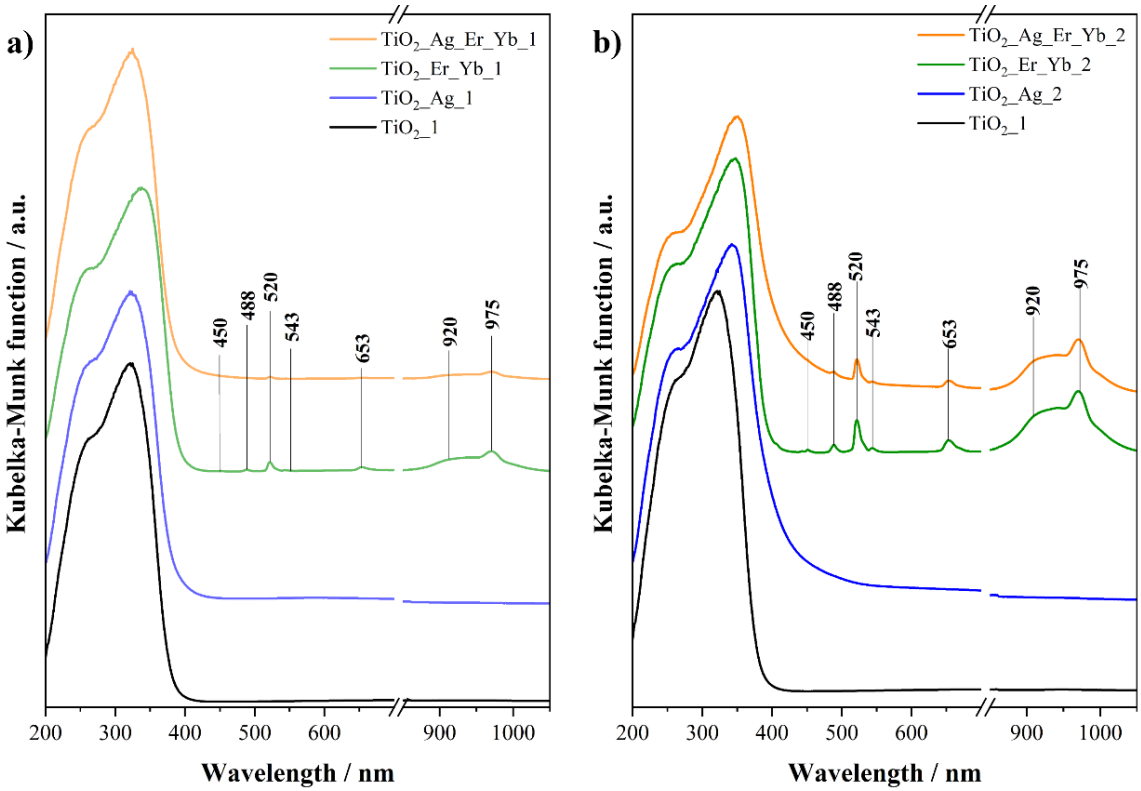

Figure 24. *DR UV-Vis-NIR spectra of the samples prepared by Method 1 (a) and the samples prepared by Method 2 (b), with the undoped TiO_2 spectra included as reference*

3.1.6 Photoluminescence (PL) spectroscopy

PL spectroscopy was employed to further investigate the optical properties of the doped TiO_2 NPs. In particular, this analysis aimed to: (i) identify the characteristic emission bands of Er^{3+} and Yb^{3+} under different excitation wavelengths, confirming their successful optical activation and assess the occurrence and direction of energy transfer processes between TiO_2, Er^{3+}, and Yb^{3+} by selectively exciting either the semiconductor matrix or the rare-earth ions. To this end, both emission and excitation spectra were collected. The instrumental parameters, including the excitation and emission wavelength ranges, slit widths, and optical filters, were optimized for each measurement to maximize the quality and information content of the acquired spectra. Since different instrumental settings were employed for the various measurements, all spectra were normalized to their maximum intensity to enable a reliable qualitative comparison of the collected data. The emission spectra were collected using the following excitation wavelengths:

- Around 345 nm, corresponding to TiO_2 band gap absorption wavelength;
- 520 nm, corresponding to the Er^{3+} green absorption;
- 975 nm, corresponding to the Er^{3+} and Yb^{3+} NIR absorption.

The excitation spectra were registered monitoring the emission at:

- 1035 nm, corresponding to the Yb^{3+} NIR emission;
- 1532 nm, corresponding to the Er^{3+} NIR emission.

Ag-doped samples were not included in this analysis due to their pronounced photo-sensitivity, which significantly affected their PL characterization.

3.1.6.1 Photoemission spectra

Figure 25 (a-b) reports the emission spectra of TiO_2_Er_2, TiO_2_Er_Yb_1 and TiO_2_Er_Yb_2, registered under direct excitation of Er^{3+} at 520 nm. Figure 17a exhibits the emission spectra in the Vis region, while Figure 17b displays the corresponding NIR emission spectra. Under this excitation wavelength, the TiO_2_Er_2 spectra (yellow) exhibits the characteristic Er^{3+} emission bands in both the visible and near-infrared regions. In particular the following transitions are observed:

- 550 - 570 nm: complex band ascribable to $^4S_{3/2} \rightarrow {}^4I_{15/2}$
- 659 nm: $^4F_{9/2} \rightarrow {}^4I_{15/2}$
- 979 nm: $^4I_{11/2} \rightarrow {}^4I_{15/2}$
- 1450 - 1640 nm: complex band ascribable to $^4I_{13/2} \rightarrow {}^4I_{15/2}$

These characteristic Er^{3+} emission bands are also observed in the co-doped Er^{3+}/Yb^{3+} samples. In addition, a broad emission band extending from approximately 975 to 1050 nm appears, which can be attributed to Yb^{3+} emission. The main components of this band are:

- 979 nm: electronic transition from the fifth Stark sublevel of the excited $^2F_{5/2}$ state to the first Stark sublevel of the ground $^2F_{7/2}$ state.
- 1008 nm: electronic transition from the fifth Stark sublevel of the excited $^2F_{5/2}$ state to the second Stark sublevel of the ground $^2F_{7/2}$ state.[50,51]

Since the applied excitation wavelength directly populates the excited states of Er^{3+} rather than Yb^{3+}, the observation of Yb^{3+} emission suggests the presence of energy transfer mechanism from Er^{3+} to Yb^{3+}. This will be further discussed in the following sections.

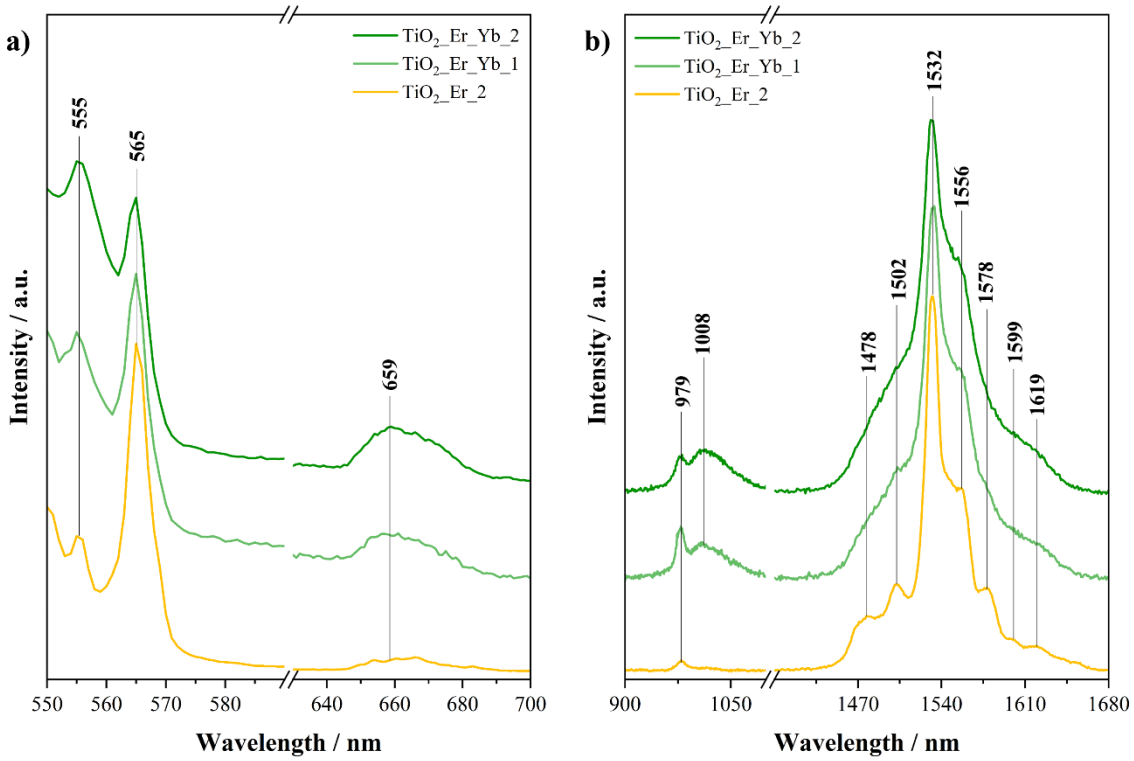

Figure 25. *PL emission spectra of TiO_2_Er_2, TiO_2_Er_Yb_1, and TiO_2_Er_Yb_2 recorded under direct excitation at 520 nm. (a) UV–Vis emission spectra. (b) NIR emission spectra. *The spectra have been normalized between 0 and 1.*

Figure 26 reports the emission spectra of TiO_2_Er_2, TiO_2_Er_Yb_1 and TiO_2_Er_Yb_2, recorded under excitation at 975 nm. The broad emission band in the 1450–1640 nm range attributed previously to the $^4I_{13/2} \rightarrow {}^4I_{15/2}$ Er^{3+} transition is observed. Since excitation at 975 nm can simultaneously address both the $^4I_{15/2} \rightarrow {}^4I_{11/2}$ transition of Er^{3+} and the $^2F_{7/2} \rightarrow {}^2F_{5/2}$ transition of Yb^{3+}, these spectra alone do not provide conclusive evidence of an energy transfer process between Yb^{3+} and Er^{3+}.

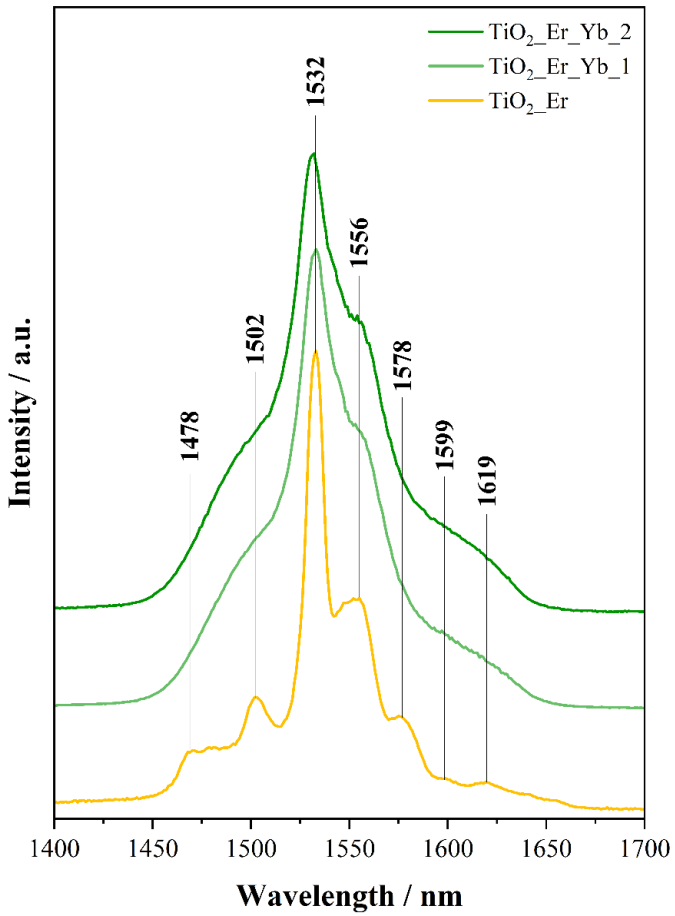

Figure 26. *PL NIR emission spectra of TiO_2_Er_2, TiO_2_Er_Yb_1, and TiO_2_Er_Yb_2 recorded under direct excitation at 975 nm. *The spectra have been normalized between 0 and 1.*

Figure 27 (a,b) reports the PL emission spectra of TiO_2_1, TiO_2_Er_2, TiO_2_Yb_2, TiO_2_Er_Yb_1, and TiO_2_Er_Yb_2 recorded under excitation at the absorption maximum of the TiO_2 matrix. Figure 27a shows that all the samples exhibit the broad emission band centred around 510 nm, which is attributed to the intrinsic photoluminescence of TiO_2.[42,43] In addition, the TiO_2_Er_2 sample displays the same Er^{3+} emission peaks previously discussed in Figure 25a. The observation of Er^{3+} emission upon excitation of TiO_2 band gap suggests that the excitation energy can be transferred from TiO_2 to Er^{3+}. Conversely, these characteristic Er^{3+} emissions are no longer observed in the co-doped samples, suggesting that under TiO_2 excitation the energy transfer towards Er^{3+} becomes less efficient in the presence of Yb^{3+}. This interpretation is further supported by the NIR spectra shown in Figure 27b. As expected, undoped TiO_2 does not exhibit any emission in this spectral region. TiO_2_Er_2 shows the broad emission band between 1450 and 1640 nm, previously assigned to the $^4I_{13/2} \rightarrow {}^4I_{15/2}$ transition of Er^{3+},

whereas TiO_2_Yb_2 displays the characteristic Yb^{3+} emission centred between approximately 975 and 1050 nm, corresponding to the $^2F_{5/2} \rightarrow {}^2F_{7/2}$ transition. These results demonstrate that the excited TiO_2 matrix is able to transfer energy to both Er^{3+} and Yb^{3+} ions. For the co-doped samples, emission bands from both Er^{3+} and Yb^{3+} are observed. However, the Yb^{3+} emission is significantly more intense than the Er^{3+} emission. Moreover, the relative Er^{3+} emission intensity is markedly lower than that observed in Figure 25b, where Er^{3+} was directly excited at 520 nm. Under TiO_2 excitation, these observations indicate that energy transfer from TiO_2 preferentially occurs towards Yb^{3+} rather than Er^{3+}. This behaviour is consistent with the larger absorption cross-section of Yb^{3+} and with its ten times higher concentration than Er^{3+}, both of which increase the probability of $TiO_2 \rightarrow Yb^{3+}$ energy transfer.[48,50]

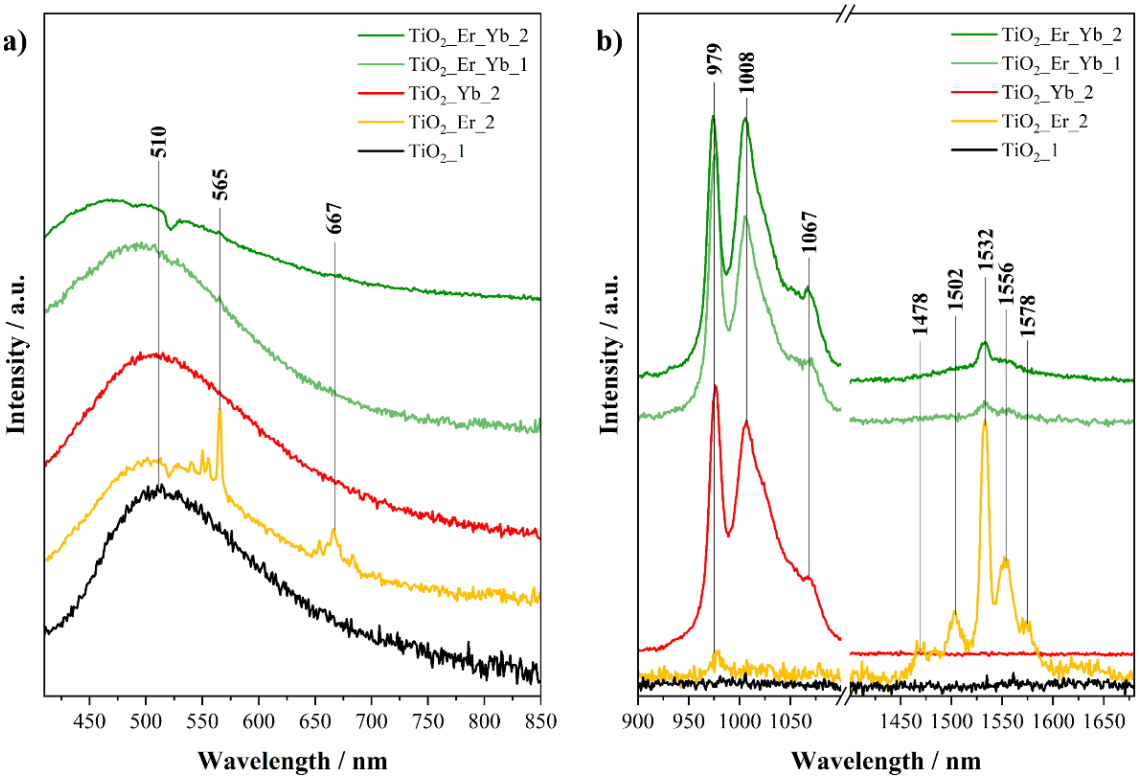

Figure 27. *PL emission spectra of TiO_2_1, TiO_2_Er_2, TiO_2_Er_Yb_1, and TiO_2_Er_Yb_2 recorded under direct excitation at 345 nm, 343 nm, 338 nm, and 348 nm, respectively. (a) UV–Vis emission spectra. (b) NIR emission spectra. *The spectra have been normalized between 0 and 1.*

3.1.6.2 Photoexcitation spectra

Figure 28 (a-b) reports the excitation spectra recorded monitoring the characteristics NIR emission wavelengths of Er^{3+} at 1532 nm and of Yb^{3+} at 1035 nm. The emission

wavelength of 1532 nm was selected because it corresponds to the most intense component of the Er^{3+} NIR emission band observed in Figures 10 and 11. For Yb^{3+}, the emission was monitored at 1035 nm instead of the maximum at approximately 979 nm, since the latter overlaps with the Er^{3+} emission arising from the $^4I_{11/2} \rightarrow {}^4I_{15/2}$ transition, reported in Figure 25b and 27b. Monitoring at 1035 nm therefore ensures that only the Yb^{3+} emission is detected.

Figure 28a shows the excitation spectra of TiO_2_Er_2, TiO_2_Er_Yb_1 and TiO_2_Er_Yb_2 collected by monitoring the Er^{3+} emission at 1532 nm. The spectra exhibit the characteristic Er^{3+} absorption bands previously discussed in Figure 20. In addition, two absorption bands centred at approximately 381 and 408 nm become clearly visible, that corresponds to the following transitions:[48]

- 381 nm: $^4I_{15/2} \rightarrow {}^4G_{11/2}$
- 408 nm: $^4I_{15/2} \rightarrow {}^2H_{9/2}$

These transitions were not distinguishable in the DR UV–Vis–NIR spectra because they were masked by the strong absorption of the TiO_2 matrix. Furthermore, a weak broad excitation band extending from approximately 300 to 400 nm is observed. This band is characteristic of TiO_2 absorption and, since the monitored emission originates from Er^{3+}, its presence demonstrates that excitation of the TiO_2 matrix contributes to the Er^{3+} emission, providing further evidence of energy transfer from TiO_2 to Er^{3+}. Interestingly, the TiO_2-related excitation band is slightly more pronounced for the mono-doped Er^{3+} sample than for the co-doped materials. This observation is consistent with the PL spectra reported in Figure 25a, where the characteristic visible Er^{3+} emission is observed only for TiO_2_Er_2 under TiO_2 excitation. These results suggest that the presence of Yb^{3+} reduces the efficiency of the $TiO_2 \rightarrow Er^{3+}$ energy transfer.

Figure 28b reports the excitation spectra of TiO_2_Yb_2, TiO_2_Er_Yb_1 and TiO_2_Er_Yb_2 recorded by monitoring the Yb^{3+} emission at 1035 nm. All samples exhibit the intense broad excitation band between approximately 300 and 400 nm, corresponding to the intrinsic absorption of TiO_2. Since the detected emission originates from Yb^{3+}, this feature provides clear evidence that the excitation energy absorbed by the TiO_2 matrix is efficiently transferred to Yb^{3+} ions. In the co-doped samples, the excitation spectra also display the characteristic Er^{3+} absorption bands. Since the monitored emission exclusively arises from Yb^{3+}, these features indicate that excitation of Er^{3+} can populate

the excited states of Yb^{3+}, confirming the occurrence of energy transfer between Er^{3+} and Yb^{3+} ions.

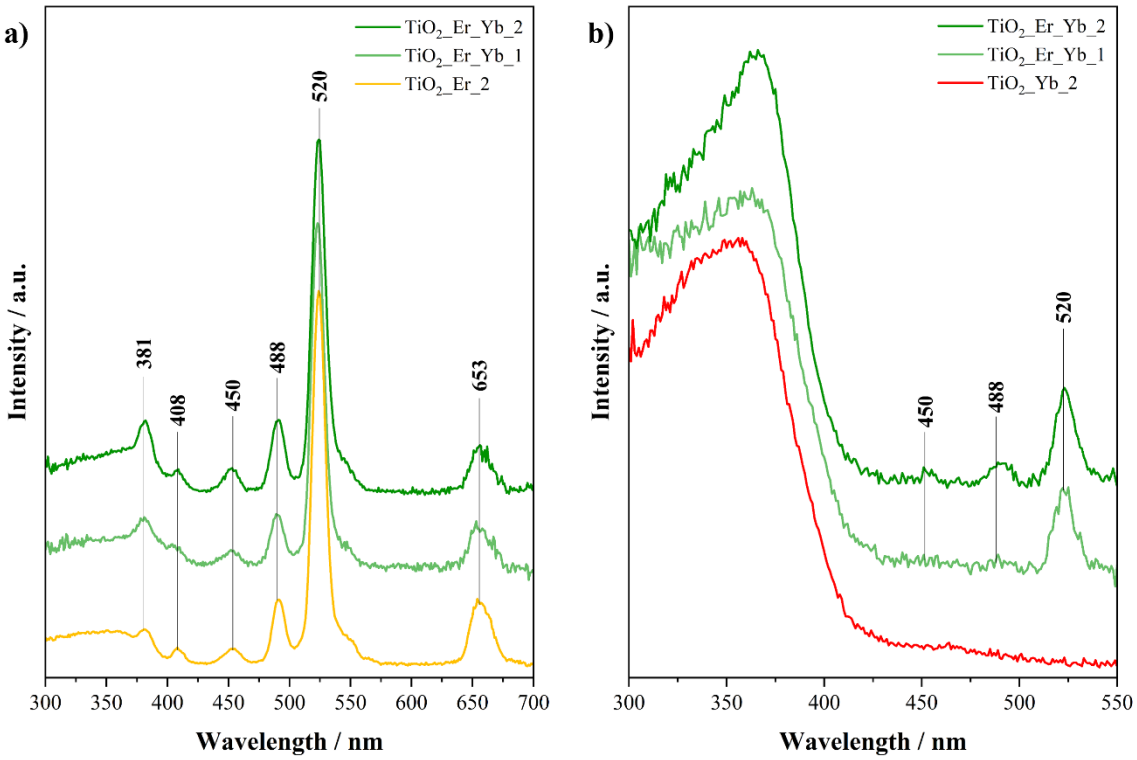

Figure 28. *a) PL excitation spectra of TiO_2_Er_2, TiO_2_Er_Yb_1, and TiO_2_Er_Yb_2 recorded monitoring the emission wavelength at 1532 nm; (b) PL excitation spectra of TiO_2_Yb_2, TiO_2_Er_Yb_1, and TiO_2_Er_Yb_2 recorded monitoring the emission wavelength at 1035 nm.*The spectra have been normalized between 0 and 1.*

In conclusion, PL analysis provided a coherent picture of the energy transfer processes occurring in the synthesized doped TiO_2 NPs. The emission and excitation spectra suggests that the TiO_2 matrix is able to transfer excitation energy to both Er^{3+} and Yb^{3+}. In the co-doped samples, however, energy transfer from TiO_2 preferentially occurs towards Yb^{3+}, as evidenced by the stronger Yb^{3+} emission and the reduced Er^{3+} luminescence under TiO_2 excitation. At the same time, the observation of Er^{3+} absorption features in the excitation spectra monitored at the Yb^{3+} emission wavelength, together with the Yb^{3+} emission under direct Er^{3+} excitation, suggests the occurrence of energy transfer between Er^{3+} and Yb^{3+}. These findings outline a possible network of energy transfer pathways operating in the co-doped systems, where energy transfer occurs between Er^{3+} and Yb^{3+} in both directions, while TiO_2 can sensitize both rare-earth ions, with a preferential $TiO_2 \rightarrow Yb^{3+}$ pathway thanks to the larger absorption cross-section of Yb^{3+} and its higher concentration than Er^{3+}.

3.1.7 Upconversion (UC)

The upconversion (UC) properties of the synthesized nanoparticles were finally investigated through optical characterization. Since the proposed system relies on the NIR-to-Vis UC in order to activate TiO_2, photoluminescence spectroscopy was employed to assess the optical response of the rare-earth-doped samples under 980 nm excitation. In particular, the measurements aimed to verify the successful optical activation of Er^{3+} and Yb^{3+} ions and to evaluate the effectiveness of the Er^{3+}/Yb^{3+} upconversion process.

Figure 29a reports the emission spectra collected in the range 500-700 nm of TiO_2_1, TiO_2_Ag_2 and TiO_2_Ag_1, upon irradiation with a 980 nm laser. As expected, none of these samples exhibit detectable upconversion emission, since they do not contain optically active rare-earth ions capable of converting near-infrared radiation into visible light. The recorded spectra are characterized only by a weak and nearly featureless background, confirming that the introduction of Ag alone does not induce upconversion behaviour in TiO_2.

Figure 29b compares the emission spectra of undoped TiO_2 and mono-doped Er^{3+} TiO_2 collected under the same experimental conditions. While the undoped sample does not exhibit any significant emission, the TiO_2_Er_2 sample displays the characteristic upconversion luminescence of Er^{3+}, consisting of two broad emission bands located in the green (520–570 nm) and red (640–690 nm) spectral regions, corresponding to the following Er^{3+} transitions:[48,52,53]

- 520-570 nm: $^2H_{11/2} \rightarrow {}^4I_{15/2}$ and $^4S_{3/2} \rightarrow {}^4I_{15/2}$
- 640-690 nm: $^4F_{9/2} \rightarrow {}^4I_{15/2}$

This observation indicates that Er^{3+} ions are able to generate upconversion luminescence even in the absence of Yb^{3+}. This is in accordance with the literature, where upconversion in Er^{3+}-only systems mainly occurs through the Excited State Absorption (ESA) mechanism, in which the sequential absorption of two 980 nm photons by the same Er^{3+}

ion promotes the population of the excited states responsible for the green and red emissions.[16]

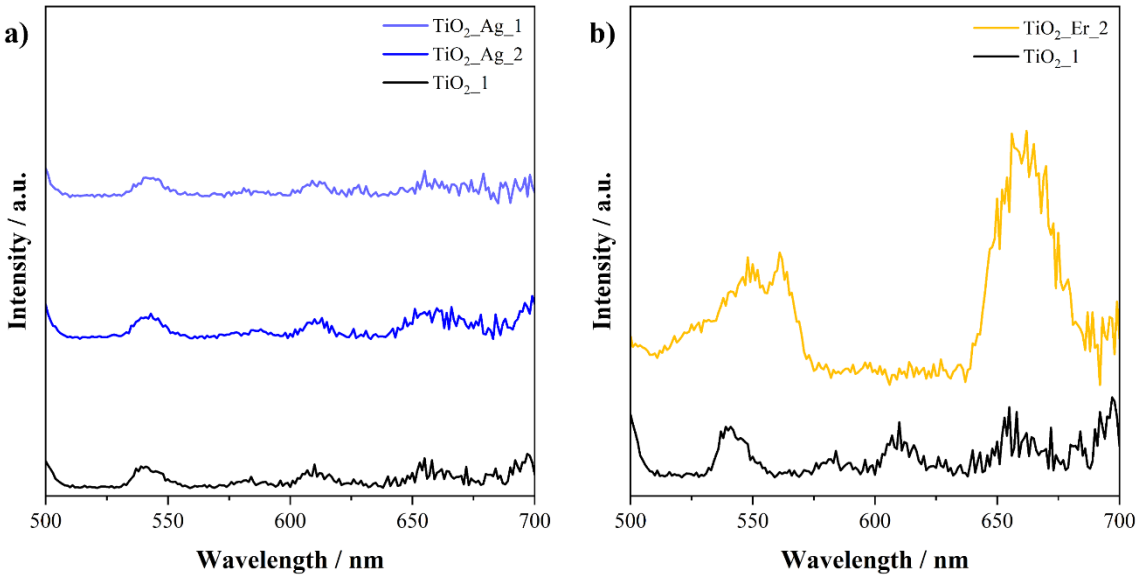

Figure 29. *UC emission spectra upon irradiation at 980 nm with a laser power of 1240 mW (1430 mA). (a) TiO_2_1, TiO_2_Ag_2 and TiO2_Ag_1 samples, (b) TiO_2_1 and TiO_2_Er_2 samples.*

Figure 30 (a-b) reports the UC emission spectra of the co-doped Er^{3+}/Yb^{3+} samples under 980 nm excitation. All the samples exhibit the same green and red emission bands already observed for the Er^{3+} sample, confirming that the UC emission still originates from the characteristic Er^{3+} transitions. However, a remarkable increase in the emission intensity is observed after the introduction of Yb^{3+}, particularly for the red emission around 660 nm. This enhancement is consistent with the well-known sensitizing role of Yb^{3+} ions. Compared to Er^{3+}, Yb^{3+} possesses a much larger absorption cross-section at 980 nm and can efficiently transfer the absorbed energy to Er^{3+} ions that are close in space. As a result, the population of the Er^{3+} excited states becomes more efficient, leading to an overall increase in the UC emission intensity.

Although all the co-doped samples exhibit the same spectral profile, differences in the overall emission intensity can be observed. In particular, TiO_2_Ag_Er_Yb_1 shows the highest UC emission intensity, whereas TiO_2_Er_Yb_2 exhibits the lowest one.

No significant differences can be observed between the Ag-containing and Ag-free samples, suggesting that the presence of Ag clusters does not substantially affect the UC emission under the investigated experimental conditions.

These results confirm that the presence of Yb^{3+} improves the upconversion efficiency by acting as an effective sensitizer for Er^{3+}, leading to a more efficient population of the emitting states compared to the Er^{3+} only samples.[48,50]

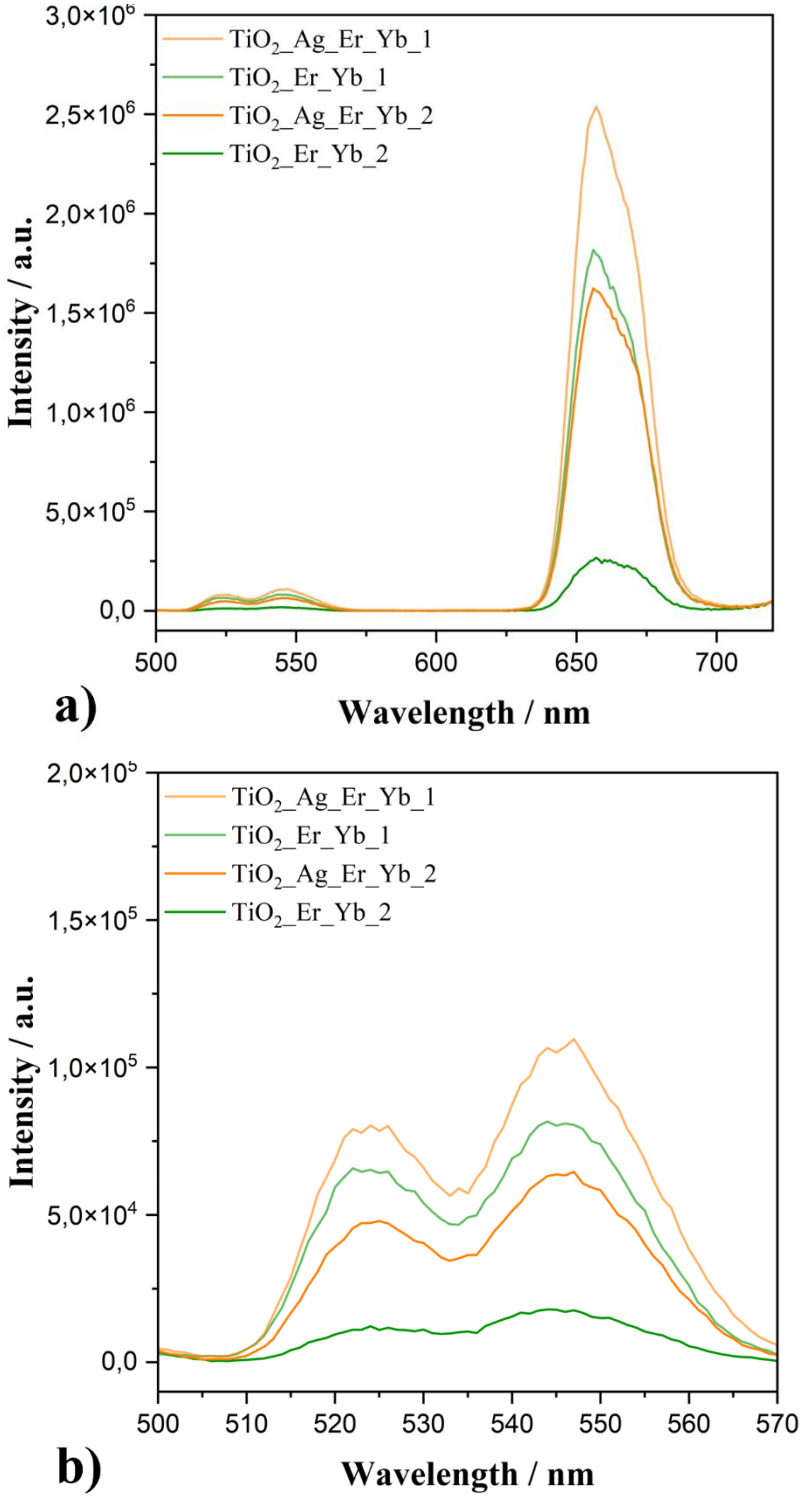

Figure 30. *UC emission spectra of TiO_2_Er_Yb_1, TiO_2_Er_Yb_2, TiO_2_Ag_Er_Yb_1 and TiO_2_Ag_Er_Yb_2, upon irradiation at 980 nm. (b) zoom of the green emission region.*

To provide a quantitative comparison of the upconversion emission, the green and red bands were integrated, and the corresponding areas are reported in Table 5. The results confirm the qualitative observations from Figure 22 (a-b), showing noticeable differences in the overall emission intensity among the investigated samples. In particular, TiO_2_Ag_Er_Yb_1 exhibits the largest integrated emission in both spectral regions, whereas TiO_2_Er_Yb_2 shows the lowest values. Despite these differences in absolute intensity, the green-to-red integrated area ratio remains relatively constant for all the samples, ranging from approximately 0.045 to 0.073.

***Table 4**. Integration value of the area of the green emission band and the red emission band for TiO2_Er_Yb_1, TiO2_Er_Yb_2, TiO2_Ag_Er_Yb_1 and TiO2_Ag_Er_Yb_2 with the respective green/red ratio*

Sample	Green emission area	Red emission area	Green/Red
TiO_2_Er_Yb_1	2.83×10^6	5.10×10^7	0.0556
TiO_2_Er_Yb_2	5.72×10^5	7.81×10^6	0.0732
TiO_2_Ag_Er_Yb_2	2.10×10^6	4.71×10^7	0.0446
TiO_2_Ag_Er_Yb_1	3.60×10^6	7.14×10^7	0.0505

3.1.8 Reactive oxygen species (ROS) generation tests

To investigate the ability of the synthesized TiO_2 nanoparticles to generate reactive oxygen species (ROS), oxidation experiments were performed using 1,3-diphenylisobenzofuran (DPBF) as a chemical probe. According to the literature, DPBF is a highly sensitive molecule that can be readily oxidized in the presence of photo-generated reactive species. DPBF exhibits a characteristic absorption band centred at around 411 nm, which does not overlap with the absorption bands of the doped TiO_2 nanoparticles.

Upon reaction with ROS, DPBF undergoes a [4+2] cycloaddition reaction, leading to the formation of an unstable endoperoxide intermediate. This intermediate subsequently degrades to 1,2-dibenzoylbenzene (DBB). The reaction disrupts the conjugated π-system of DPBF, causing a progressive decrease in the intensity of its characteristic visible absorption band. Therefore, the decrease in DPBF absorbance can be used as an indirect

indication of ROS generation by the investigated nanoparticles. The reaction mechanism is reported in Figure 22.[54,55]

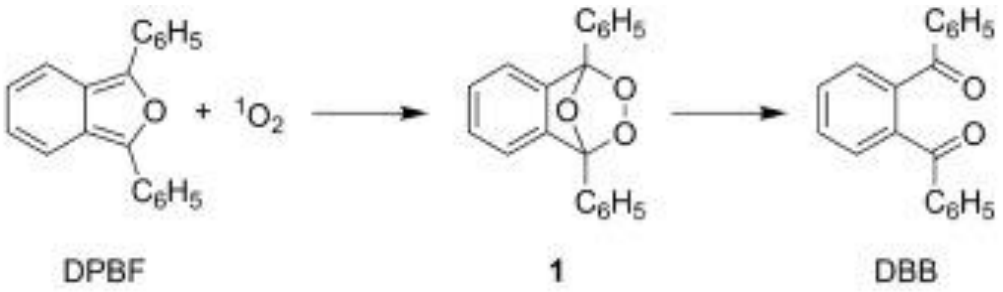

Figure 31. *Reaction mechanism of $^1O_2$ with DPBF.*[54]

The experiments were carried out according to the procedure described in the Materials and Methods section.

Figure 33 (a-d) reports the UV–Vis spectra of the DPBF solution (a), TiO_2_Er_Yb_1 (b), TiO_2_Ag_Er_Yb_1 (c), and TiO_2_Ag_Er_Yb_2 (d) under 520 nm irradiation. The spectra were collected after 0, 5, 15, 30, and 60 min of irradiation. For all the investigated samples, no significant decrease in the DPBF absorption band at 411 nm was observed over the irradiation time. The DPBF solution showed no appreciable spectral variation, confirming that DPBF is stable under 520 nm irradiation in the absence of nanoparticles. Similarly, the spectra collected in the presence of the selected TiO_2 samples did not show a significant decrease in DPBF absorbance. These results indicate that, under 520 nm irradiation and under the adopted experimental conditions, no detectable ROS generation occurred. Therefore, direct excitation of Er^{3+} at this wavelength does not appear to provide sufficient energy transfer to the TiO_2 matrix to induce a measurable oxidation of DPBF.

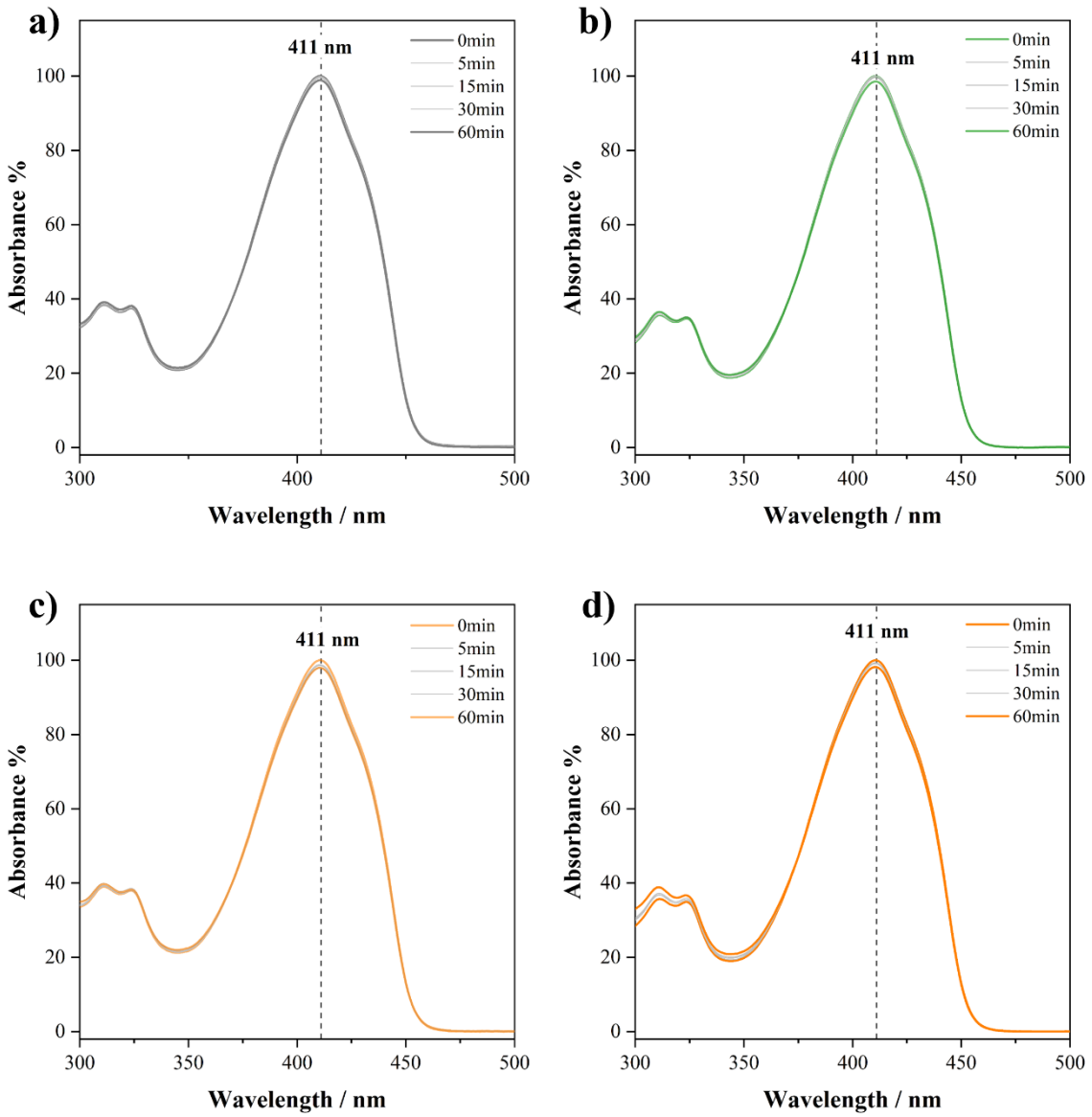

Figure 33. *UV-Vis spectra of the DPBF solution (a), TiO_2_Er_Yb_1 (b), TiO_2_Ag_Er_Yb_1 (c), TiO_2_Ag_Er_Yb_2 (d) registered after 0, 5, 15, 30, and 60 min of irradiation at 520 nm.*

Figure 34 summarizes the absorbance % values at 411 nm obtained from all the spectra reported in Figure 33. The offer clear evidence that only minor variations in the DPBF absorption band were observed during irradiation. In all cases, the absorbance remained above 98% of its initial value after 60 min, indicating that DPBF degradation was negligible under 520 nm irradiation. The small decrease observed for some samples can be attributed to the high sensitivity of DPBF towards oxidation.[54,55] However, this variation is too small to indicate a significant ROS-mediated oxidation process. Therefore, these results further confirm that no measurable photocatalytic ROS generation occurred under the adopted experimental conditions.

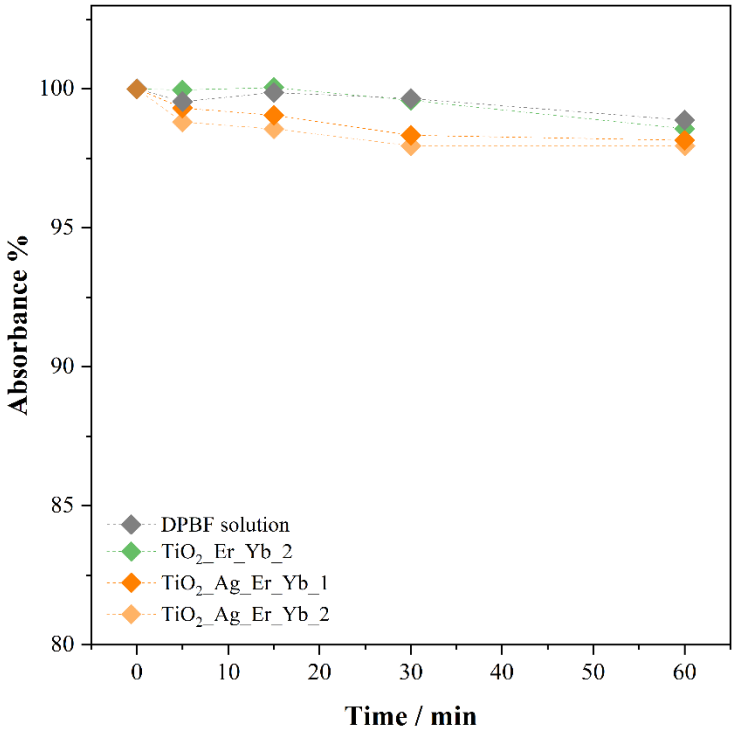

Figure 34. *Summary of the absorbance % values at 411 nm obtained from the spectra at different times of the DPBF solution and the TiO_2_Er_Yb_1, TiO_2_Ag_Er_Yb_1, TiO_2_Ag_Er_Yb_2 samples upon 520 nm irradiation.*

Figure 35 (a-e) reports the UV-Vis spectra of the DPBF solution (a), TiO_2_1 (b), TiO_2_Er_Yb_1 (c), TiO_2_Ag_Er_Yb_1 (d), and TiO_2_Ag_Er_Yb_2 (e) under 980 nm irradiation. The spectra were collected after 0, 5, 10, 15, 20, 30, 40, 50 and 60 min of irradiation. The DPBF solution (Figure 35a) doesn't exhibits a significant variation of the characteristic DPBF absorption band at 411 nm over 60 min of irradiation, confirming that DPBF is stable under near-infrared light in the absence of nanoparticles. In the presence of TiO_2_1 (Figure 35b), the intensity of the DPBF absorption band remains almost unchanged, suggesting that the undoped sample does not is not effective for ROS generation under the adopted experimental conditions. On the other hand, a progressive decrease in the absorbance at 411 nm is observed for TiO_2_Er_Yb_1 (Figure 35c), TiO_2_Ag_Er_Yb_1 (Figure 35d), and TiO_2_Ag_Er_Yb_2 (Figure 35e). The decrease is more pronounced for TiO_2_Ag_Er_Yb_2, indicating a higher DPBF oxidation efficiency under 980 nm irradiation.

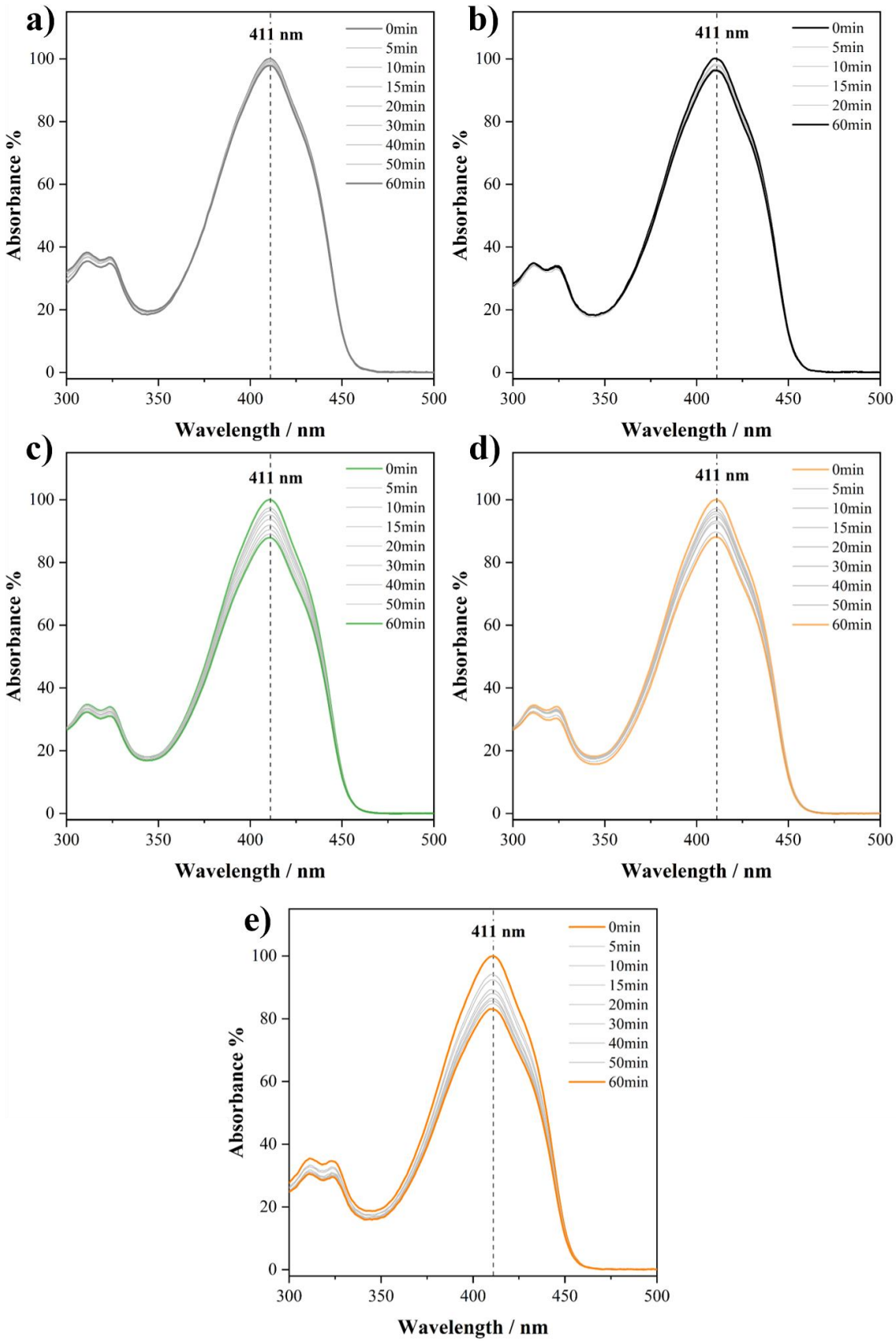

Figure 35. *UV-Vis spectra of the DPBF solution (a), TiO_2_1 (b), TiO_2_Er_Yb_1 (c), TiO_2_Ag_Er_Yb_1 (d), TiO_2_Ag_Er_Yb_2 (e) registered after 0, 5, 10, 15, 20, 30, 40, 50 and 60 min of irradiation at 980 nm.*

Figure 36 summarizes the absorbance % values at 411 nm obtained from all the spectra reported in Figure 35, allowing a direct comparison of the different samples. As expected, the DPBF solution and undoped TiO_2_1 show only minor absorbance variations over the irradiation time. Among the rare-earth-containing samples, TiO_2_Ag_Er_Yb_2 shows the most pronounced decrease, reaching approximately 83% of its initial absorbance after 60 min. TiO_2_Er_Yb_1 and TiO_2_Ag_Er_Yb_1 show a less pronounced but still progressive decrease, reaching final absorbance values close to 88%. Overall, the graph highlights the different DPBF oxidation efficiencies of the investigated samples and identifies TiO_2_Ag_Er_Yb_2 as the most effective formulation under the adopted experimental conditions.

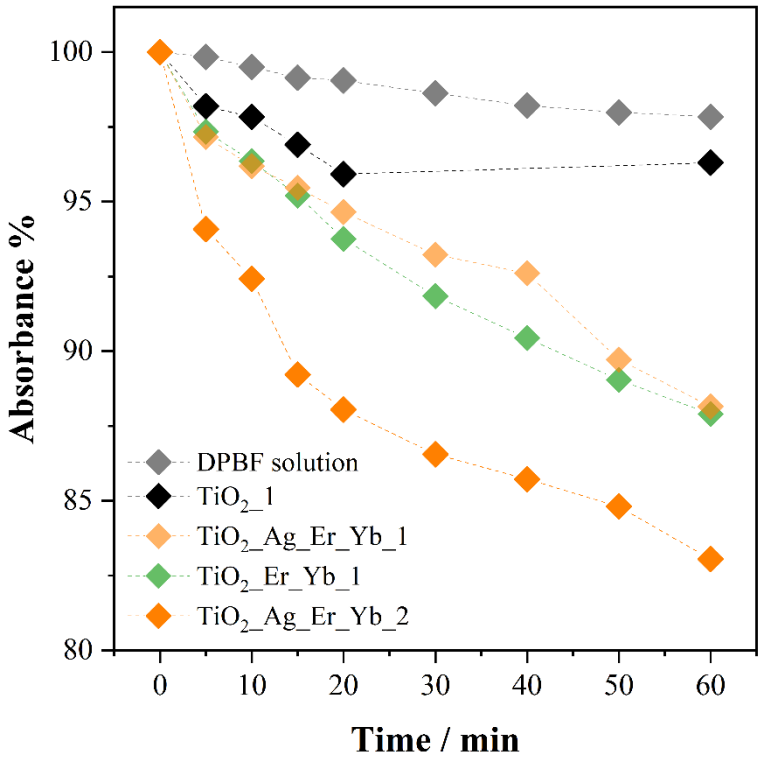

Figure 36. *Summary of the absorbance % values at 411 nm obtained from the spectra at different times of the DPBF solution and the TiO_2_1, TiO_2_Er_Yb_1, TiO_2_Ag_Er_Yb_1, TiO_2_Ag_Er_Yb_2 samples upon 980 nm irradiation.*

Finally, Figure 37 offer a clear comparison between the percentage decrease in DPBF absorbance at 411 nm after 60 min of irradiation at 520 and 980 nm. Under 520 nm irradiation, all the investigated systems show only minor absorbance variations, ranging from 1 to 2%. This result confirms that direct visible excitation does not lead to a measurable photo-oxidation of DPBF under the adopted experimental conditions. On the

other hand, under 980 nm irradiation, the rare-earth-containing samples show a markedly higher decrease in DPBF absorbance. TiO_2_Er_Yb_1 and TiO_2_Ag_Er_Yb_1 both induce a 12% decrease, whereas TiO_2_Ag_Er_Yb_2 shows the highest value, reaching a 17% decrease after 60 min. The DPBF solution, used as a control, shows only a 2% variation under the same irradiation conditions.

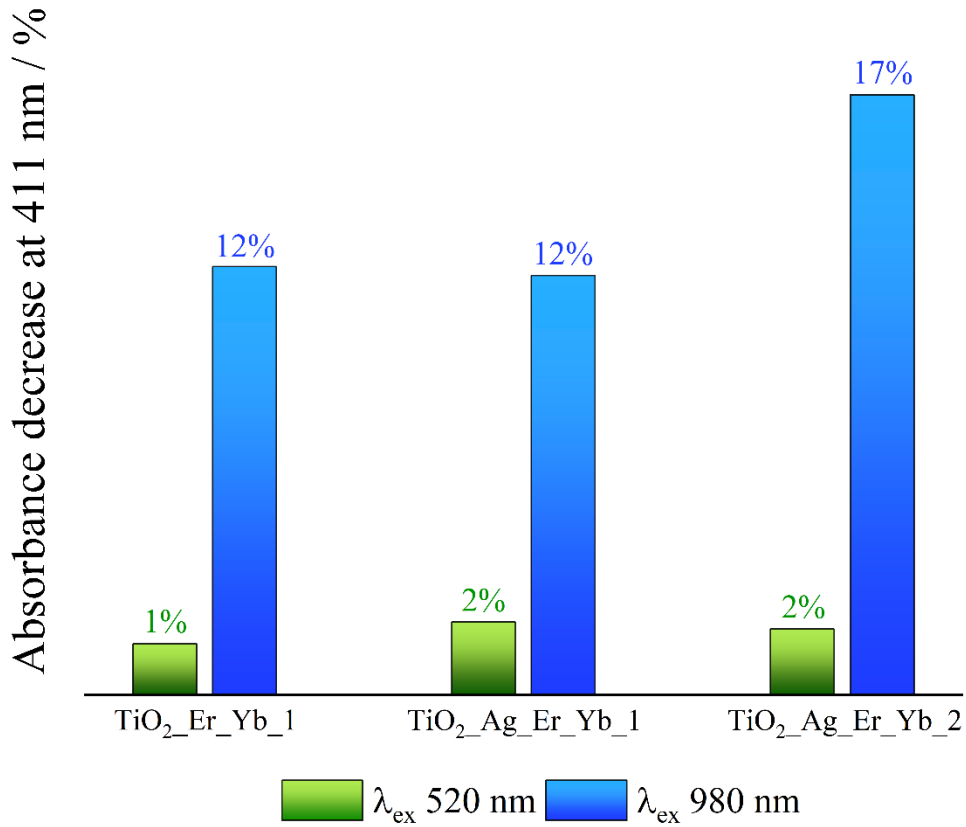

Figure 37. *Percentage decrease in DPBF absorbance at 411 nm after 60 min of irradiation at 520 nm and 980 nm for the TiO_2_Er_Yb_1, TiO_2_Ag_Er_Yb_1 and TiO_2_Ag_Er_Yb_2 samples*

In conclusion, these results demonstrate that the Er^{3+}/Yb^{3+} upconversion process play a key role in enabling the activation of TiO_2 under 980 nm excitation and therefore inducing the oxidation of DPBF through ROS generation. Moreover, the higher DPBF decrease observed for TiO_2_Ag_Er_Yb_2 is consistent with the DR UV-Vis-NIR data that showed a wider TiO_2 band gap shift for the TiO_2_Ag_Er_Yb_2 sample, attesting that the Ag-induced TiO_2 band gap modification is fundamental in improving the interaction between Er^{3+} and the TiO_2 matrix.

4. Conclusions

The present thesis work focused on the design, sol-gel synthesis, and comprehensive chemical-physical and functional characterization of innovative nanostructured architectures based on co-doped titanium dioxide (TiO_2) nanoparticles with rare earth elements (Er^{3+}/Yb^{3+}) and modified with Ag. The core of the research centred on developing an advanced, multifunctional photocatalytic platform capable of overcoming the intrinsic limitations of pure TiO_2 by extending its optical activity into the near-infrared region, tailored for potential biomedical application in photodynamic therapy (PDT).

From a structural and morphological standpoint, XRPD results demonstrated that the adopted sol-gel methodology consistently isolates the anatase phase, which is universally recognized as the most photocatalytically active form of titania. Crucially, neither the sequential introduction of the metallic and rare earth dopants nor the choice of post-synthetic treatment (washing vs. non-washing) compromised the integrity of the host matrix's crystalline phase, resulting only in a minor and predictable decrease in the overall degree of crystallinity. Electron Microscopy investigations (FE-SEM and STEM), combined with DLS measurements, confirmed the development of well-defined spherical nanoparticles with primary diameters confined within the 50–100 nm range, although they exist within a reversible macro-aggregation equilibrium in aqueous environments that can be managed via mechanical filtration.

Quantitative XRF analysis revealed a pivotal detail regarding the stability of the synthetic protocol: the procedure based on Method 2 (samples not subjected to post-calcination washing) retains an absolute dopant content significantly closer to the nominal values compared to Method 1. Even though washing causes partial leaching of superficial chemical species, a highly positive outcome is that the Yb/Er molar ratio remains constant around the stoichiometric value of 10 across all studied systems. This preserves the precise spatial distance and energetic interaction between the sensitizer ion (Yb^{3+}) and the activator ion (Er^{3+}), which is a strict prerequisite for efficient upconversion energy transfer.

The efficacy of the molecular design was thoroughly corroborated by DR UV-Vis-NIR and photoluminescence studies. Diffuse reflectance spectroscopy confirmed, on one hand, the retention of the intra-4f transitions of the lanthanides (with the main band at 975 nm well-preserved and unaltered by other components) and, on the other hand,

highlighted the decisive role of silver. The incorporation of Ag generates a sharp red-shift in the semiconductor's absorption edge, expanding its action spectrum into the visible light range. This phenomenon, most prominent in the unwashed system (TiO_2_Ag_Er_Yb_2) due to its higher noble metal content, reflects the formation of Ag clusters on the particle surfaces. These clusters establish a metal-semiconductor junction (Schottky barrier) that acts as an electron sink, effectively hindering radiative recombination and increasing the quantum efficiency of the system.

Ultimately, the functional success of the proposed strategy was validated by reactive oxygen species (ROS) generation tests using DPBF as a tracer molecule. While direct stimulation in the visible region at 520 nm did not exhibit appreciable photocatalytic responses under the adopted experimental conditions, irradiation at 980 nm (NIR region) provided unequivocal proof of the indirect activation of TiO_2. The upconversion mechanism of the Er^{3+}/Yb^{3+} pair successfully converts low-energy infrared photons into transitions capable of driving redox processes on the catalyst's surface, steering the oxidative degradation of the probe. In line with the structural and optical evidence, the unwashed sample TiO_2_Ag_Er_Yb_2 displayed the superior functional performance, inducing a 17% reduction of the DPBF signal within 60 minutes.

In conclusion, the optimized nanostructured architecture TiO_2_Ag_Er_Yb_2 successfully meets all the predefined requirements. It proves that the co-presence of the upconversion system and silver clusters synergistically extends the photoactivity of titanium dioxide into the near-infrared therapeutic window. This study establishes a robust foundation for the future deployment of these nanoplatforms in nanomedicine, where the deep tissue penetration enabled by NIR light, combined with the proven capacity for in situ ROS generation, holds great promise for utilizing these materials as innovative agents in cancer photodynamic therapy.

References

(1) Chauhan, D. S.; Prasad, R.; Dhanka, M.; Kaur, N.; Vithalani, H.; Liyanapathirana, K.; Hebbandi Nanjundappa, R.; Gao, H.; Umeshappa, C. S. Nanoparticles-Based Phototherapy Systems: Molecular Mechanisms and Clinical Applications. *Signal Transduct. Target. Ther.* **2026**, *11* (1), 95. https://doi.org/10.1038/s41392-025-02536-w.

(2) Chen, G.; Qiu, H.; Prasad, P. N.; Chen, X. Upconversion Nanoparticles: Design, Nanochemistry, and Applications in Theranostics. *Chem. Rev.* **2014**, *114* (10), 5161–5214. https://doi.org/10.1021/cr400425h.

(3) Manekar, B. A.; Patil, S. R.; Akpan, U. G. Comparative Study of Doped and Co-Doped TiO2 for Photocatalytic Degradation of Organic Pollutant: A Review. *Chem. Eng. J. Adv.* **2026**, *27*, 101288. https://doi.org/10.1016/j.ceja.2026.101288.

(4) Mazierski, P.; Mikolajczyk, A.; Bajorowicz, B.; Malankowska, A.; Zaleska-Medynska, A.; Nadolna, J. The Role of Lanthanides in TiO2-Based Photocatalysis: A Review. *Appl. Catal. B Environ.* **2018**, *233*, 301–317. https://doi.org/10.1016/j.apcatb.2018.04.019.

(5) Mazierski, P.; Nischk, M.; Gołkowska, M.; Lisowski, W.; Gazda, M.; Winiarski, M. J.; Klimczuk, T.; Zaleska-Medynska, A. Photocatalytic Activity of Nitrogen Doped TiO2 Nanotubes Prepared by Anodic Oxidation: The Effect of Applied Voltage, Anodization Time and Amount of Nitrogen Dopant. *Appl. Catal. B Environ.* **2016**, *196*, 77–88. https://doi.org/10.1016/j.apcatb.2016.05.006.

(6) Mazierski, P.; Lisowski, W.; Grzyb, T.; Winiarski, M. J.; Klimczuk, T.; Mikołajczyk, A.; Flisikowski, J.; Hirsch, A.; Kołakowska, A.; Puzyn, T.; Zaleska-Medynska, A.; Nadolna, J. Enhanced Photocatalytic Properties of Lanthanide-TiO2 Nanotubes: An Experimental and Theoretical Study. *Appl. Catal. B Environ.* **2017**, *205*, 376–385. https://doi.org/10.1016/j.apcatb.2016.12.044.

(7) Reszczyńska, J.; Grzyb, T.; Wei, Z.; Klein, M.; Kowalska, E.; Ohtani, B.; Zaleska-Medynska, A. Photocatalytic Activity and Luminescence Properties of RE3+–TiO2 Nanocrystals Prepared by Sol–Gel and Hydrothermal Methods. *Appl. Catal. B Environ.* **2016**, *181*, 825–837. https://doi.org/10.1016/j.apcatb.2015.09.001.

(8) Jadhav, A. J.; Goswami, A. D.; Trivedi, D. H.; Chavan, P. V.; Jadhav, N. L.; Pinjari, D. V. A Comprehensive Review on Pure and Doped Titanium Oxide Nanoparticles for Photocatalytic Applications. *Inorg. Chem. Commun.* **2025**, *181*, 115206. https://doi.org/10.1016/j.inoche.2025.115206.

(9) Guo, Q.; Zhou, C.; Ma, Z.; Yang, X. Fundamentals of TiO_2 Photocatalysis: Concepts, Mechanisms, and Challenges. *Adv. Mater.* **2019**, *31* (50), 1901997. https://doi.org/10.1002/adma.201901997.

(10) Gupta, S. M.; Tripathi, M. A Review of TiO2 Nanoparticles. *Chin. Sci. Bull.* **2011**, *56* (16), 1639–1657. https://doi.org/10.1007/s11434-011-4476-1.

(11) 'Aliaa Razali, N.; Amira Othman, S. Sol-Gel Technique in Study of Titanium Dioxide (TiO2) Photocatalytic Activity- a Short Review. *Mater. Today Proc.* **2022**, *66*, 4077–4083. https://doi.org/10.1016/j.matpr.2022.07.150.

(12) Etacheri, V.; Di Valentin, C.; Schneider, J.; Bahnemann, D.; Pillai, S. C. Visible-Light Activation of TiO2 Photocatalysts: Advances in Theory and Experiments. *J. Photochem. Photobiol. C Photochem. Rev.* **2015**, *25*, 1–29. https://doi.org/10.1016/j.jphotochemrev.2015.08.003.

(13) Nawaz, M. N.; Zhang, Z.; Yuan, W.; Khan, S. B. Photocatalytic Enhancement of TiO2 through Silver, Gold, and Platinum Doping. *Energy Nexus* **2025**, *19*, 100495. https://doi.org/10.1016/j.nexus.2025.100495.

(14) Goryacheva, O. A.; Beloglazova, N. V.; Vostrikova, A. M.; Pozharov, M. V.; Sobolev, A. M.; Goryacheva, I. Yu. Lanthanide-to-Quantum Dot Förster Resonance Energy Transfer (FRET): Application for Immunoassay. *Talanta* **2017**, *164*, 377–385. https://doi.org/10.1016/j.talanta.2016.11.054.

(15) Le, X. T.; Youn, Y. S. Emerging NIR Light-Responsive Delivery Systems Based on Lanthanide-Doped Upconverting Nanoparticles. *Arch. Pharm. Res.* **2020**, *43* (1), 134–152. https://doi.org/10.1007/s12272-020-01208-3.

(16) Cheng, X.; Zhou, J.; Yue, J.; Wei, Y.; Gao, C.; Xie, X.; Huang, L. Recent Development in Sensitizers for Lanthanide-Doped Upconversion Luminescence. *Chem. Rev.* **2022**, *122* (21), 15998–16050. https://doi.org/10.1021/acs.chemrev.1c00772.

(17) Tu, L.; Liu, X.; Wu, F.; Zhang, H. Excitation Energy Migration Dynamics in Upconversion Nanomaterials. *Chem. Soc. Rev.* **2015**, *44* (6), 1331–1345. https://doi.org/10.1039/C4CS00168K.

(18) Liang, L.; Qin, X.; Zheng, K.; Liu, X. Energy Flux Manipulation in Upconversion Nanosystems. *Acc. Chem. Res.* **2019**, *52* (1), 228–236. https://doi.org/10.1021/acs.accounts.8b00469.

(19) Yaqoob, A. A.; Ahmad, H.; Parveen, T.; Ahmad, A.; Oves, M.; Ismail, I. M. I.; Qari, H. A.; Umar, K.; Mohamad Ibrahim, M. N. Recent Advances in Metal Decorated Nanomaterials and Their Various Biological Applications: A Review. *Front. Chem.* **2020**, *8*, 341. https://doi.org/10.3389/fchem.2020.00341.

(20) Lu, S.; Wu, D.; Wang, Q.; Yan, J.; Buekens, A. G.; Cen, K. Photocatalytic Decomposition on Nano-TiO2: Destruction of Chloroaromatic Compounds. *Chemosphere* **2011**, *82* (9), 1215–1224. https://doi.org/10.1016/j.chemosphere.2010.12.034.

(21) Amin, S. A.; Pazouki, M.; Hosseinnia, A. Synthesis of TiO2–Ag Nanocomposite with Sol–Gel Method and Investigation of Its Antibacterial Activity against E. Coli. *Powder Technol.* **2009**, *196* (3), 241–245. https://doi.org/10.1016/j.powtec.2009.07.021.

(22) Huan, Y.; Xuxu, Z.; Zhongyi, Y.; Feng, T. Preparation of Nitrogen-Doped Ti02 Nanoparticle Catalyst and Its CatalyticActivity under Visible Light. **2007**.

(23) Diwald, O.; Thompson, T. L.; Zubkov, T.; Ed. G. Goralski,; Walck, S. D.; Yates, J. T. Photochemical Activity of Nitrogen-Doped Rutile TiO_2 (110) in Visible Light. *J. Phys. Chem. B* **2004**, *108* (19), 6004–6008. https://doi.org/10.1021/jp031267y.

(24) Livraghi, S.; Paganini, M. C.; Giamello, E.; Selloni, A.; Di Valentin, C.; Pacchioni, G. Origin of Photoactivity of Nitrogen-Doped Titanium Dioxide under Visible Light. *J. Am. Chem. Soc.* **2006**, *128* (49), 15666–15671. https://doi.org/10.1021/ja064164c.

(25) Correia, J. H.; Rodrigues, J. A.; Pimenta, S.; Dong, T.; Yang, Z. Photodynamic Therapy Review: Principles, Photosensitizers, Applications, and Future Directions. *Pharmaceutics* **2021**, *13* (9), 1332. https://doi.org/10.3390/pharmaceutics13091332.

(26) Yoo, S. W.; Oh, G.; Ahn, J. C.; Chung, E. Non-Oncologic Applications of Nanomedicine-Based Phototherapy. *Biomedicines* **2021**, *9* (2), 113. https://doi.org/10.3390/biomedicines9020113.

(27) Przygoda, M.; Bartusik-Aebisher, D.; Dynarowicz, K.; Cieślar, G.; Kawczyk-Krupka, A.; Aebisher, D. Cellular Mechanisms of Singlet Oxygen in Photodynamic Therapy. *Int. J. Mol. Sci.* **2023**, *24* (23), 16890. https://doi.org/10.3390/ijms242316890.

(28) 1. Photodynamic Therapy for Cancer.

(29) Santos, L. M.; Machado, W. A.; França, M. D.; Borges, K. A.; Paniago, R. M.; Patrocinio, A. O. T.; Machado, A. E. H. Structural Characterization of Ag-Doped TiO_2 with Enhanced Photocatalytic Activity. *RSC Adv.* **2015**, *5* (125), 103752–103759. https://doi.org/10.1039/C5RA22647C.

(30) Di Valentin, C.; Pacchioni, G.; Selloni, A.; Livraghi, S.; Giamello, E. Characterization of Paramagnetic Species in N-Doped TiO_2 Powders by EPR Spectroscopy and DFT Calculations. *J. Phys. Chem. B* **2005**, *109* (23), 11414–11419. https://doi.org/10.1021/jp051756t.

(31) Di Valentin, C.; Finazzi, E.; Pacchioni, G.; Selloni, A.; Livraghi, S.; Paganini, M. C.; Giamello, E. N-Doped TiO2: Theory and Experiment. *Chem. Phys.* **2007**, *339* (1–3), 44–56. https://doi.org/10.1016/j.chemphys.2007.07.020.

(32) Gaggero, E.; Giovagnoni, A.; Zollo, A.; Calza, P.; Paganini, M. C. Photocatalytic Degradation of Emerging Contaminants with N-Doped TiO2 Using Simulated Sunlight in Real Water Matrices. *Inorganics* **2023**, *11* (11), 439. https://doi.org/10.3390/inorganics11110439.

(33) Livraghi, S.; Czoska, A. M.; Paganini, M. C.; Giamello, E. Preparation and Spectroscopic Characterization of Visible Light Sensitized N Doped TiO2 (Rutile). *J. Solid State Chem.* **2009**, *182* (1), 160–164. https://doi.org/10.1016/j.jssc.2008.10.012.

(34) Di Valentin, C.; Pacchioni, G.; Selloni, A. Reduced and N-Type Doped TiO_2 : Nature of Ti^{3+} Species. *J. Phys. Chem. C* **2009**, *113* (48), 20543–20552. https://doi.org/10.1021/jp9061797.

(35) Bezerra, P.; Cavalcante, R.; Garcia, A.; Wender, H.; Martines, M.; Casagrande, G.; Giménez, J.; Marco, P.; Oliveira, S.; Machulek Jr., A. Synthesis, Characterization, and Photocatalytic Activity of Pure and N-, B-, or Ag- Doped TiO2. *J. Braz. Chem. Soc.* **2017**. https://doi.org/10.21577/0103-5053.20170040.

(36) Wang, K.; Zhuo, Y.; Chen, J.; Gao, D.; Ren, Y.; Wang, C.; Qi, Z. Crystalline Phase Regulation of Anatase–Rutile TiO_2 for the Enhancement of Photocatalytic Activity. *RSC Adv.* **2020**, *10* (71), 43592–43598. https://doi.org/10.1039/D0RA09421H.

(37) Mustapha, S.; Tijani, J. O.; Ndamitso, M. M.; Abdulkareem, A. S.; Shuaib, D. T.; Amigun, A. T.; Abubakar, H. L. Facile Synthesis and Characterization of TiO2 Nanoparticles: X-Ray Peak Profile Analysis Using Williamson–Hall and Debye–Scherrer Methods. *Int. Nano Lett.* **2021**, *11* (3), 241–261. https://doi.org/10.1007/s40089-021-00338-w.

(38) Jawale, N. S.; Arbuj, S. S.; Umarji, G. G.; Rane, S. B. Synthesis of Anatase/Brookite Mixed Phase TiO_2 Nanostructures and Its Photocatalytic Performance Study. *ChemistrySelect* **2021**, *6* (33), 8861–8867. https://doi.org/10.1002/slct.202102349.

(39) Alam, Md. A.; Ahmed, S.; Bishwas, R. K.; Mostofa, S.; Jahan, S. A. X-Ray Crystallographic Diffraction Study by Whole Powder Pattern Fitting (WPPF) Method: Refinement of Crystalline Nanostructure Polymorphs TiO2. *South Afr. J. Chem. Eng.* **2025**, *51*, 68–77. https://doi.org/10.1016/j.sajce.2024.10.010.

(40) Ikram, M.; Umar, E.; Raza, A.; Haider, A.; Naz, S.; Ul-Hamid, A.; Haider, J.; Shahzadi, I.; Hassan, J.; Ali, S. Dye Degradation Performance, Bactericidal Behavior and Molecular Docking Analysis of Cu-Doped TiO_2 Nanoparticles. *RSC Adv.* **2020**, *10* (41), 24215–24233. https://doi.org/10.1039/D0RA04851H.

(41) Yadav, V.; Saini, V. K.; Sharma, H. How Different Dopants Leads to Difference in Photocatalytic Activity in Doped TiO2? *Ceram. Int.* **2020**, *46* (17), 27308–27317. https://doi.org/10.1016/j.ceramint.2020.07.216.

(42) Ali, T.; Ahmed, A.; Alam, U.; Uddin, I.; Tripathi, P.; Muneer, M. Enhanced Photocatalytic and Antibacterial Activities of Ag-Doped TiO2 Nanoparticles under Visible Light. *Mater. Chem. Phys.* **2018**, *212*, 325–335. https://doi.org/10.1016/j.matchemphys.2018.03.052.

(43) Xin, B.; Jing, L.; Ren, Z.; Wang, B.; Fu, H. Effects of Simultaneously Doped and Deposited Ag on the Photocatalytic Activity and Surface States of TiO_2. *J. Phys. Chem. B* **2005**, *109* (7), 2805–2809. https://doi.org/10.1021/jp0469618.

(44) Seery, M. K.; George, R.; Floris, P.; Pillai, S. C. Silver Doped Titanium Dioxide Nanomaterials for Enhanced Visible Light Photocatalysis. *J. Photochem. Photobiol. Chem.* **2007**, *189* (2–3), 258–263. https://doi.org/10.1016/j.jphotochem.2007.02.010.

(45) Chen, G.; Qiu, H.; Prasad, P. N.; Chen, X. Upconversion Nanoparticles: Design, Nanochemistry, and Applications in Theranostics. *Chem. Rev.* **2014**, *114* (10), 5161–5214. https://doi.org/10.1021/cr400425h.

(46) Gogoi, D.; Namdeo, A.; Golder, A. K.; Peela, N. R. Ag-Doped TiO2 Photocatalysts with Effective Charge Transfer for Highly Efficient Hydrogen Production through Water Splitting. *Int. J. Hydrog. Energy* **2020**, *45* (4), 2729–2744. https://doi.org/10.1016/j.ijhydene.2019.11.127.

(47) Bezerra, P.; Cavalcante, R.; Garcia, A.; Wender, H.; Martines, M.; Casagrande, G.; Giménez, J.; Marco, P.; Oliveira, S.; Machulek Jr., A. Synthesis, Characterization, and Photocatalytic Activity of Pure and N-, B-, or Ag- Doped TiO2. *J. Braz. Chem. Soc.* **2017**. https://doi.org/10.21577/0103-5053.20170040.

(48) Miletto, I.; Gionco, C.; Paganini, M. C.; Cerrato, E.; Marchese, L.; Gianotti, E. Red Upconverter Nanocrystals Functionalized with Verteporfin for Photodynamic Therapy Triggered by Upconversion. *Int. J. Mol. Sci.* **2022**, *23* (13), 6951. https://doi.org/10.3390/ijms23136951.

(49) Reszczyńska, J.; Grzyb, T.; Sobczak, J. W.; Lisowski, W.; Gazda, M.; Ohtani, B.; Zaleska, A. Visible Light Activity of Rare Earth Metal Doped (Er3+, Yb3+ or Er3+/Yb3+) Titania Photocatalysts. *Appl. Catal. B Environ.* **2015**, *163*, 40–49. https://doi.org/10.1016/j.apcatb.2014.07.010.

(50) Nicorelli, A. Materiali upconverter a base di nanoparticelle di biossido di Titanio drogate con ioni lantanidi.

(51) Tesi Marzetti (1).

(52) Shang, Q.; Yu, H.; Kong, X.; Wang, H.; Wang, X.; Sun, Y.; Zhang, Y.; Zeng, Q. Green and Red Up-Conversion Emissions of Er3+–Yb3+ Co-Doped TiO2 Nanocrystals Prepared by Sol–Gel Method. *J. Lumin.* **2008**, *128* (7), 1211–1216. https://doi.org/10.1016/j.jlumin.2007.11.097.

(53) Baldini, D. C.; De Faria, E. H.; Ciuffi, K. J.; Rocha, L. A.; Nassar, E. J. TiO2 Films Obtained by the Sol–Gel Process and Doped with Yb3+ and Er3+ Ions. *J. Sol-Gel Sci. Technol.* **2021**, *97* (3), 548–555. https://doi.org/10.1007/s10971-020-05465-y.

(54) Entradas, T.; Waldron, S.; Volk, M. The Detection Sensitivity of Commonly Used Singlet Oxygen Probes in Aqueous Environments. *J. Photochem. Photobiol. B* **2020**, *204*, 111787. https://doi.org/10.1016/j.jphotobiol.2020.111787.

(55) Nsubuga, A.; Mandl, G. A.; Capobianco, J. A. Investigating the Reactive Oxygen Species Production of Rose Bengal and Merocyanine 540-Loaded Radioluminescent Nanoparticles. *Nanoscale Adv.* **2021**, *3* (5), 1375–1381. https://doi.org/10.1039/D0NA00964D.